Thermal Analysis of Biochemical Systems

by

Scott Jacob McEuen

Submitted to the Department of Mechanical Engineering
in partial fulfillment of the requirements for the degree of

Doctor of Philosophy

at the

MASSACHUSETTS INSTITUTE OF TECHNOLOGY

June 2013

ARCHIVES

MASSACHUSETTS INSTITUTE OF TECHNOLOGY

JUN 2 5 2013

LIBRARIES

© Massachusetts Institute of Technology 2013. All rights reserved.

Author .....
Department of Mechanical Engineering
May 7, 2013

Certified by .....
Ian Hunter
Hatsopoulos Professor of Mechanical Engineering
Thesis Supervisor

Accepted by .....
David Hardt
Chairman, Department Committee on Graduate Students

Thermal Analysis of Biochemical Systems

by

Scott Jacob McEuen

Submitted to the Department of Mechanical Engineering
on May 7, 2013, in partial fulfillment of the
requirements for the degree of
Doctor of Philosophy

Abstract

Scientists, both academic and industrial, develop two main types of drugs: 1) small molecule drugs, which are usually chemically synthesized and are taken orally and 2) large molecule, biotherapeutic, or protein-based drugs, which are often synthesized via ribosome transcription in bacteria cells and are injected. Historically, the majority of drug development, revenue, and products has come from small molecule drugs. However, recently biotherapeutic drugs have become more common due to their increased potency and specificity (the ability to chemically bond to the targeted protein of interest). Researchers now estimate that as much as 50% of current drug development activities (pre-market approval) are focused on these protein-based drugs.

There are several well-documented steps necessary in the development of a new large molecule drug. One critical element during the end of the biotherapeutic drug discovery phase and the beginning of the manufacturing phase is known as preformulation or formulation development. During this stage scientists systematically test the effects of adding various excipients (non-protein additives added to enhance the protein stability, solubility, activity of the drug, etc.) to the potential large molecule drug. Differential scanning calorimetry (DSC) is a common technique used to perform these formulation studies.

In a classic DSC experiment, a protein is heated from 20-80^{0}C and the heat absorbed while the protein unfolds is measured. Many researchers prefer the use of a DSC instrument because of its label-free nature, meaning that no fluorescent or radio-labeled tag is necessary to perform the measurement. The heat absorbed during the unfolding event(s) is directly measured. However, current commercial DSC instruments suffer from high protein consumption (especially when compared to other labeled techniques), low sensitivity, and slow throughput.

The aim of this thesis is to address two of the three areas mentioned above: high protein consumption and slow throughput. Since many formulation development studies are performed at therapeutic or high protein concentrations, one can reduce the experimental cell volume and thereby reduce the amount of protein material consumed. However, since there is less sample, less heat is produced. While in the

literature there are several heat transfer models that describe how a DSC instrument functions, there are surprisingly few heat transfer models that detail how ambient temperature disturbances impact the thermal measurement. To better describe this behavior, a simplified state-space thermal model was created to predict the disturbance rejection of a custom DSC instrument. This model was verified experimentally using linear stochastic system identification techniques.

To reduce sample throughput, the prototype calorimeter cell was made from disposable materials. Because the majority of protein systems are thermodynamically irreversible, at elevated temperatures the protein solution often aggregates and needs to be cleaned before a subsequent experiment can be run. This cleaning process constitutes a significant portion of the overall time to run an experiment. This thesis documents a fully functional DSC instrument that, while not completely disposable, has been designed, built, and tested with disposable microfluidic materials. Future work would then solve the technical hurdles of repeatably loading disposable microfluidic cells into the DSC instrument.

Thesis Supervisor: Ian Hunter
Title: Hatsopoulos Professor of Mechanical Engineering

Acknowledgments

To Maren, without whom this would not have been possible.

Contents

List of Figures

List of Tables

Chapter 1

Introduction

To introduce the topic of this thesis, the development of a new differential scanning calorimeter, it is important to provide context with respect to the use of calorimetry in the life sciences. As a result, this introductory chapter is split into the following three sections:

- Drug development
- Calorimetry
- Differential scanning calorimetry applications

1.1 Drug Development

According to the United States Food and Drug Administration (FDA) a drug is defined as follows [4]:

- A substance recognized by an official pharmacopoeia or formulary.
- A substance intended for use in the diagnosis, cure, mitigation, treatment, or prevention of disease.
- A substance (other than food) intended to affect the structure or any function of the body.

- A substance intended for use as a component of a medicine but not a device or a component, part or accessory of a device.

- Biological products are included within this definition and are generally covered by the same laws and regulations, but differences exist regarding their manufacturing processes (chemical process versus biological process.)

Proteins are responsible for controlling and regulating human body functions and are therefore the target of any drug. There are two broad categories of drugs: agonists and antagonists. An agonist drug chemically binds to a protein to facilitate a normal protein function. An antagonist drug chemically binds to a protein of interest to prevent a normal protein function. For example, there are several antagonist cancer drugs that are designed to bind to the signaling protein that initiates the formation of vasculature feeding a cancerous growth or tumor. The goal is to prevent the protein from performing its natural process of signaling other proteins to start the growth of blood vessels that bring nutrients to the cancer cells.

The development of new drugs is a highly complex and risky venture. Current numbers vary, but industry experts estimate that the development of a new drug costs between $1-1.2 billion and takes 12-15 years to develop and receive regulatory approval. In addition, of the roughly 5,000-10,000 potential drug compounds that show initial promise, only five will make it to human trials, and only one will become a regulatory approved drug [1, 10, 22].

The development of a new drug can be subdivided into five major phases [22]:

- Drug discovery

- Pre-clinical trials

- Clinical trials

- Manufacturing

- Marketing/regulatory approval

Each step in the process, with the exception of drug discovery (the R&D phase of the project), is highly regulated and must conform to established regulatory laws and practices. Currently the three largest drug markets are North America, Europe, and Japan, and they are regulated by the U.S. Food and Drug Administration (FDA), the European Medicines Agency (EMEA), and Pharmaceuticals and Medical Devices Agency (PMDA) respectively. The clinical trial phase consumes about half of the total drug development time allotment and roughly one third of the total development cost [1].

At present there are two main types of drugs developed and produced: 1) small molecule drugs and 2) large molecule, biologic, biotherapeutic, or protein-based drugs. Small molecule drugs are checmically sythnesized, often taken orally, and typically smaller than 500 Da (In biochemical vocabulary a dalton, Da, is equivalent to one unified atomic mass unit, u, and is an accepted SI unit). Examples of small molecule drugs include Lipitor (cholesterol-reducing drug from Pfizer), Plavix (used to prevent blood clots from Bristol-Myers Squibb), and Nexium (acid reflux reducer from AstraZeneca).

While small molecule drugs have traditionally dominated the drug development scene, the development of biotherapeutics is on the rise. This is due to the increased potency and higher specificity (the ability to chemically bond to the targeted protein of interest) of protein-based drugs [22]. Large molecule or biologic drugs are typically larger than 1000 Da. Researchers now estimate that as much of 50% of current drug development activities are allocated to the creation of new large molecule drugs [32]. Figure 1-1 shows a graph of the approved biotherapeutic drugs over the past 30 years [25]. Examples of large molecule drugs include Enbrel (arthritis drug from Amgen/Wyeth), Herceptin (breast cancer drug from Genentech/Roche), and Avastin (colon cancer drug from Genentech/Roche). As more researchers turn to biologic drugs, scientists and engineers will develop new technologies to facilitate this development.

While the drug discovery process is similar for both small and large molecule drugs, the manufacturing of these products is significantly different. Small molecule

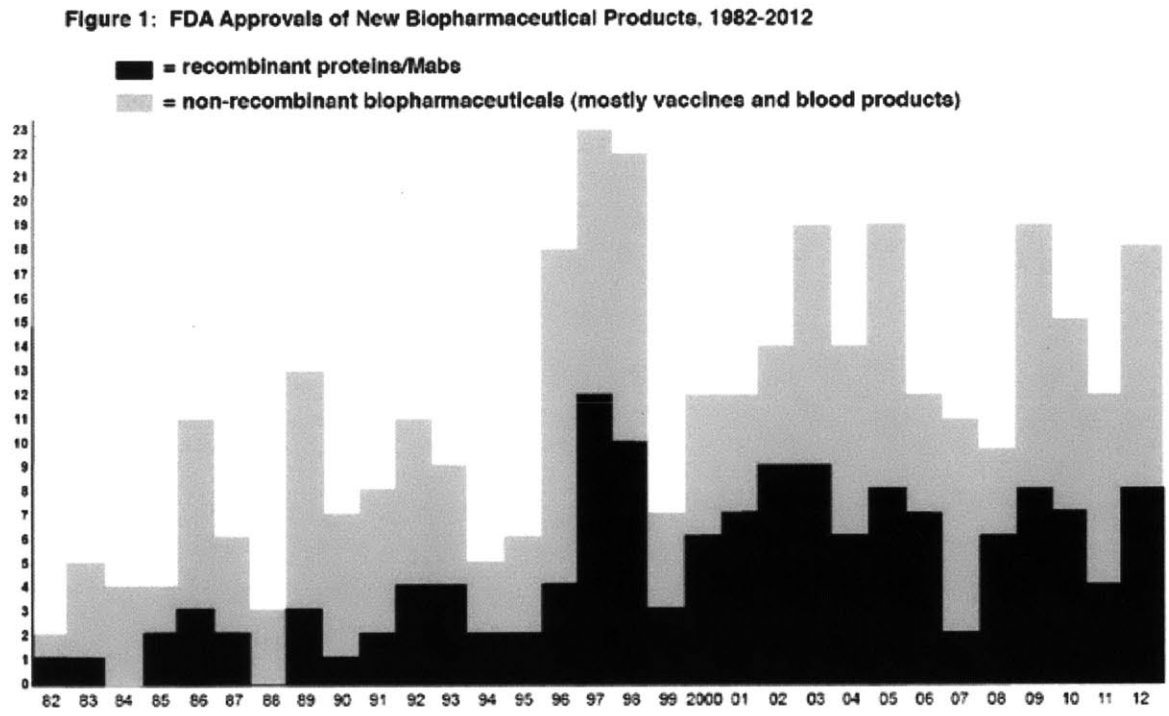

Figure 1-1: Graph showing the number of large molecule/protein-based drugs approved by the FDA [25].

drugs are chemically synthesized. Large molecule drugs are often produced through ribosome transcription in a living bacteria, mammalian, or virus cell. Then these proteins are purified from other cellular byproducts via liquid chromatography.

Differential scanning calorimetry (DSC), with respect to life sciences applications, is primarily used as an analytic tool in the development and manufacture of biotherapeutic drugs, which will be discussed in more detail in the following sections.

1.2 Calorimetry

Calorimetry is the measurement of heat. The earliest known calorimetry experiments were conducted by Joseph Black in 1760 [39]. While calorimetry is a broad technique, the following discussion will only address calorimetry as it has been applied to life sciences. There are two basic calorimetry techniques that are employed within the life sciences community: 1) isothermal titration calorimetry (ITC) and 2) differential scanning calorimetry (DSC).

Isothermal titration calorimetry was first demonstrated in a physical device in 1981 by Spokane and Gill at the University of Colorado [27]. In a traditional experiment, a potential drug compound (small or large molecule) is titrated into a solution, which contains the target protein. Equation 1.1 describes the simple equilibrium reaction. There are complex thermodynamic models that describe these reactions, but the output of an ITC measurement is the direct measurement of the binding stoichiometry, n; binding affinity or strength of the chemical bond, k_d; and the enthalpy of the reaction, h. From these parameters the entropy, S, and Gibbs free energy of the reaction, ΔG, can be calculated [27]. ITC is typically used near the end of the drug discovery phase of drug development to help researchers quantify the aforementioned attributes of the chemical reaction between the target protein and potential drug candidate.

$$A + B \rightleftharpoons AB + Q \tag{1.1}$$

where A is a protein of interest, B is a potential drug (large or small molecule),

AB is the bound protein-drug complex, and Q is the heat produced from the reaction.

Differential scanning calorimetry for life sciences applications was first developed in Russia by Privalov et al. in 1964 at the Institute of Protein Research [24]. In a routine experiment, a protein solubilized in a buffer solution is scanned from 20-80^{0}C and can be described by a simple equilibrium reaction (see Equation 1.2). Similar to ITC, there are also complex thermodynamic equations that describe the unfolding of these protein systems [5]. While Equation 1.2 shows a simple two-state transition, it is possible for a protein to exhibit multiple transitions in the midst of a temperature ramp. Each state transition is experimentally characterized by a distinct peak. Equation 1.3 contains the simplest expression for the thermodynamic equation that describes the single protein unfolding domain, named a two-state model (folded and unfolded states), and shown chemically in Equation 1.2.

$$A \rightleftharpoons A' + Q \tag{1.2}$$

where A' is a separate state of the protein A or the unfolded state of the protein.

$$C_P(T) = \frac{K_A(T)\Delta H_{mA}^2}{\left(1 + K_A(T)\right)^2 RT^2} \tag{1.3}$$

$$K_A(T) = e^{\left\{\frac{-\Delta H_{mA}}{RT}\left(1-\frac{T}{T_{mA}}\right)\right\}} \tag{1.4}$$

where H_{mA} is the enthalpy of unfolding, R is the gas constant, T is the absolute temperature, and T_{mA} is colloquially referred to as the melting temperature or more formally the temperature at which 50% of the protein has unfolded.

Figure 1-2 displays a simple two-state simulated RNase A protein unfolding experiment as described by Equation 1.3. It is common for calorimeter instruments to be calibrated using resistive heaters to display the power produced from the heat measurement. However, during data analysis, using non-linear least squares fitting techniques, power is converted to specific heat using the first law of thermodynamics (see Equation 1.7).

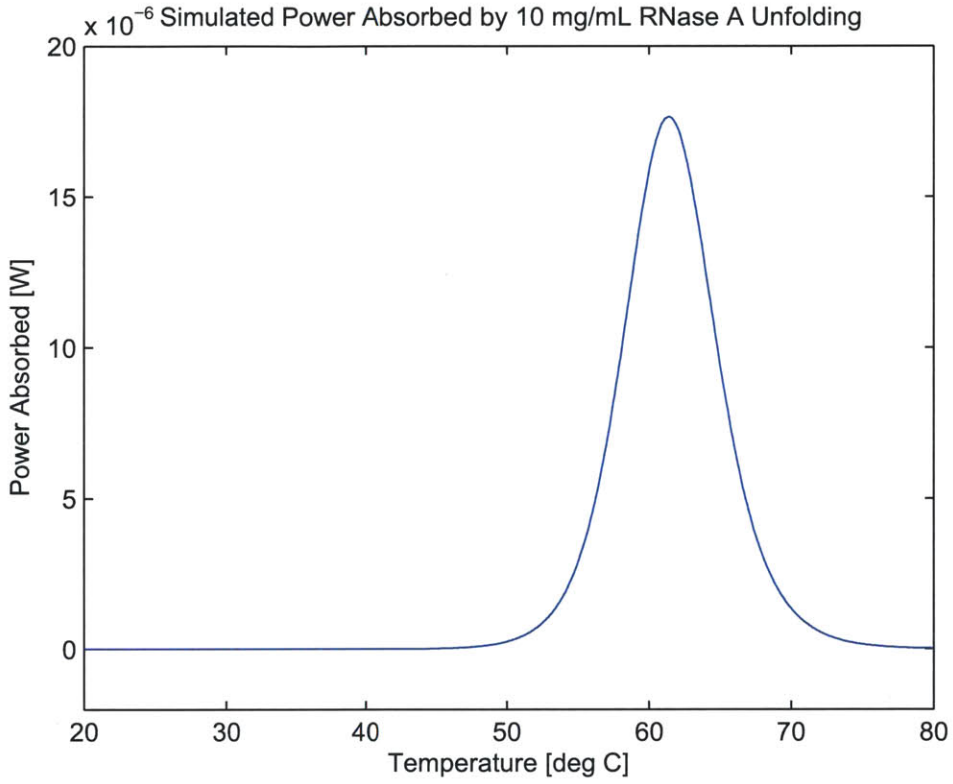

Figure 1-2: Theoretical power absorbed during RNase A protein unfolding event, the simulation based on Equation 1.3

$$\Delta U = Q + \Delta W \tag{1.5}$$

$$(mC_pT) = \left(\frac{P\Delta T}{R_{\text{scan}}}\right) + (0) \tag{1.6}$$

$$C_p = \left(\frac{P\Delta T}{mTR_{\text{scan}}}\right) \tag{1.7}$$

where ΔU is the change in internal energy of the system, Q is the heat added to the system, ΔW is work performed on the system, m is mass of the protein, C_p is the specific heat of the protein, T is the instantaneous temperature of the protein, P is the power absorbed by the protein as it unfolds, ΔT is the temperature scan range, and R_{scan} is the scan rate of the linear temperature ramp.

1.3 Calorimeter Instrument Development

As mentioned previously, calorimetry was first applied to the study of a biochemical system in 1964 [24]. Figure 1-3 shows a summary of the patents generated in the field since this early work. The majority of the early work, from the 1960s through the 1980s, was performed in the Soviet Union. Beginning in the early 1980s additional groups in the United States and Great Britain also began to develop calorimeters for the study of biomolecular interactions.

Table 1.1 displays a list of calorimeters that have been developed over the past 30 years. The sensor type, volume, and sensitivity are values reported in the cited papers. The protein consumed and protein concentrations columns represent calculated values based on RNase A protein (Sigma-Aldrich R5500) with a pH of 5.5, scanned at 200^0C/hr, and a signal-to-noise ratio of 1000:1. Although different researchers used different techniques to quantify the performance of their respective calorimeters, for a course comparison this simplistic analysis should be sufficient. While researchers often focus on volume and sensitivity, this comparison highlights some biochemical limitations, namely protein concentration. Proteins are extremely difficult to solubilize above 60 mM. These calculations suggest that many of these calorimeters would

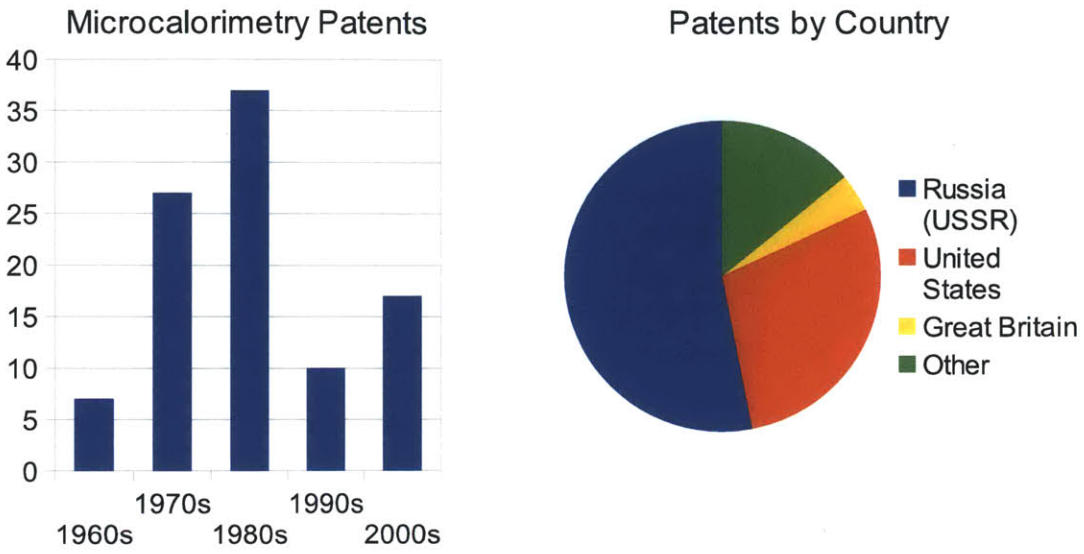

Figure 1-3: Life sciences calorimetry patents by decade and country.

not be able to perform a successful DSC measurement because a sample could not be prepared with a sufficient concentration such that it could be measured.

Figures 1-4 and 1-5 graphically display the information contained in Table 1.1. In Figure 1-4 the x-axis represents cell volume and the y-axis represents calorimeter sensitivity or noise threshold. Researchers often suggest that an ideal calorimeter would lie in the lower left portion of the plot, with low cell volume and low short-term noise. The author of this thesis does not dispute this proposition. However, this ideal does not take into consideration any biochemical limitations. Figure 1-5 plots the information to highlight those attributes that are important to a biochemical scientist, namely protein concentration and protein consumed. The x-axis represnets protein concentration and the y-axis represents protein consumed. Again, an ideal calorimeter would fall in the lower left portion of the plot. However, note the red vertical line in the plot at approximately 60 mM. This represents a conservative solubility limit for proteins. At concentrations above 60 mM it is nearly impossible to solubilize the protein. As a result, a scientist could not perform equilibrium protein unfolding experiments in a system to the right of the red line in Figure 1-5. The calorimeter described in this thesis is the only known calorimeter to the left of the

Table 1.1: Literature survey summary of life-sciences focused calorimeters. Adapted and expanded from Lee et al. 2009 [17]

Group	Sensor Type	Volume	Sensitivity	Protein Consumed	Protein Concentration	Protein Concentration
McKinnon et al. 1984 [21]	Thermopile	200 μL	250 nW	1 mg	500 uM	7 mg/mL
Wiseman et al. 1989 [38]	Bi-Te thermopile	1.4 mL	20 nW	100 μg	6 μM	0.08 mg/mL
Berger et al. 1996 [7]	Bimetallic cantilever	1 pL	1 nW	6 μg	400 M	6×10^6 mg/mL
Lerchener et al. 1999 [18]	Al-Si thermopile	6 μL	50 nW	300 μg	3 mM	50 mg/mL
Verhaegen et al. 2000 [31]	Al-Si thermopile	100 μL	1 μW	6 mg	4 mM	60 mg/mL
Johannessen et al. 2002 [15]	Au-Ni thermopile	15 nL	13 nW	70 μg	400 mM	5000 mg/mL
Zhang and Tadigadapa [41]	Au-Si thermopile	15 nL	300 nW	2 mg	8.2 M	100000 mg/mL
Chancellor et al. 2004 (cite!)	Bi-Ti thermopile	50 pL	150 nW	800 μg	1 kM	20×10^6 mg/mL
Wang et al. 2005 [36]	Bi-Te thermopile	n/a	3 nW	n/a	n/a	n/a
Baier et al. 2005 [6]	Bi-Sb thermopile	6 μL	30 nW	200 μg	2 mM	30 mg/mL
David and Hunter 2007 [9]	Liquid expansion	2 μL	n/a	n/a	n/a	n/a
Recht et al. 2008 [26]	Si thermistor	500 nL	50 nW	300 μg	40 mM	600 mg/mL
Wang et al. 2008 [34, 35]	Cr-Ni thermopile	800 nL	50 nW	300 μg	30 mM	400 mg/mL
Xu et al. 2008 [40]	Thermopile	5 nL	22 nW	100 μg	1.8 M	30000 mg/mL
Lee et al. 2009 [17]	Au-Ni thermopile	3.5 nL	4.2 nW	20 μg	500 mM	7000 mg/mL
Lubbers and Baudenbacher 2011 [20]	Bi-Sb thermopile	2.5 nL	1 nW	6 μg	200 mM	2000 mg/mL
Kopparthy et al. 2012 (cite!)	Bi-Sb thermopile	5 μL	n/a	n/a	n/a	n/a
Wang and Lin 2012 [33]	Bi-Sb thermopile	1 μL	10 nW	60 μg	4 mM	60 mg/mL
McEuen 2013	Bi-Te thermopile	10 μL	60 nW	300 μg	3 mM	30 mg/mL
GE Healthcare VP Capillary DSC	Bi-Te thermopile	135 μL	30 nW	200 μg	90 μM	1 mg/mL
TA Instruments Nano DSC	n/a	300 μL	15 nW	80 μg	20 μM	0.3 mg/mL

red line that has also been designed with disposable materials that would cost less than $10 for the disposable.

The remainder of this thesis will address the design and development of this new potentially disposable calorimeter.

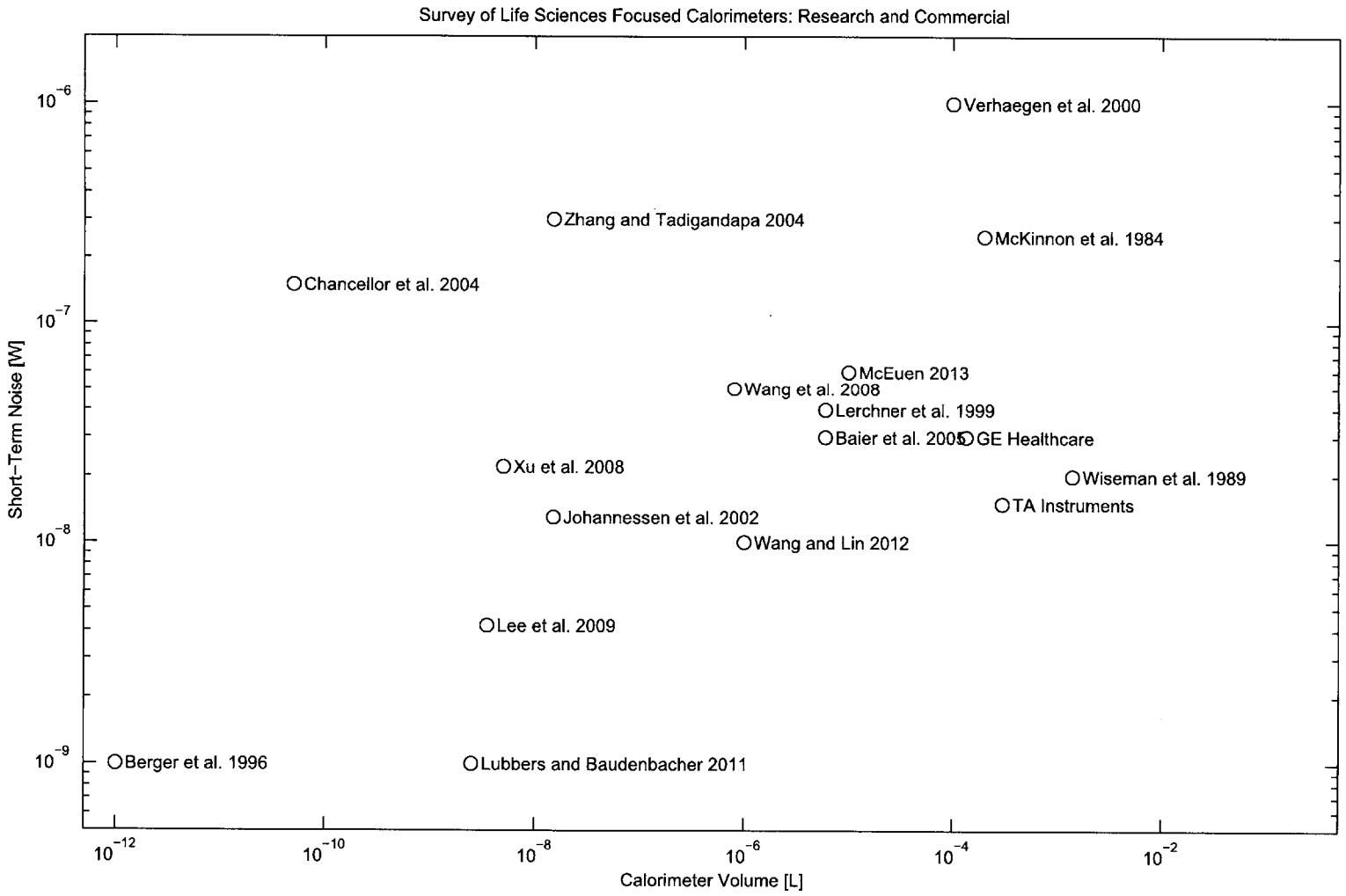

Figure 1-4: Life-sciences focused calorimeter literature survey: sensitivity vs. cell volume

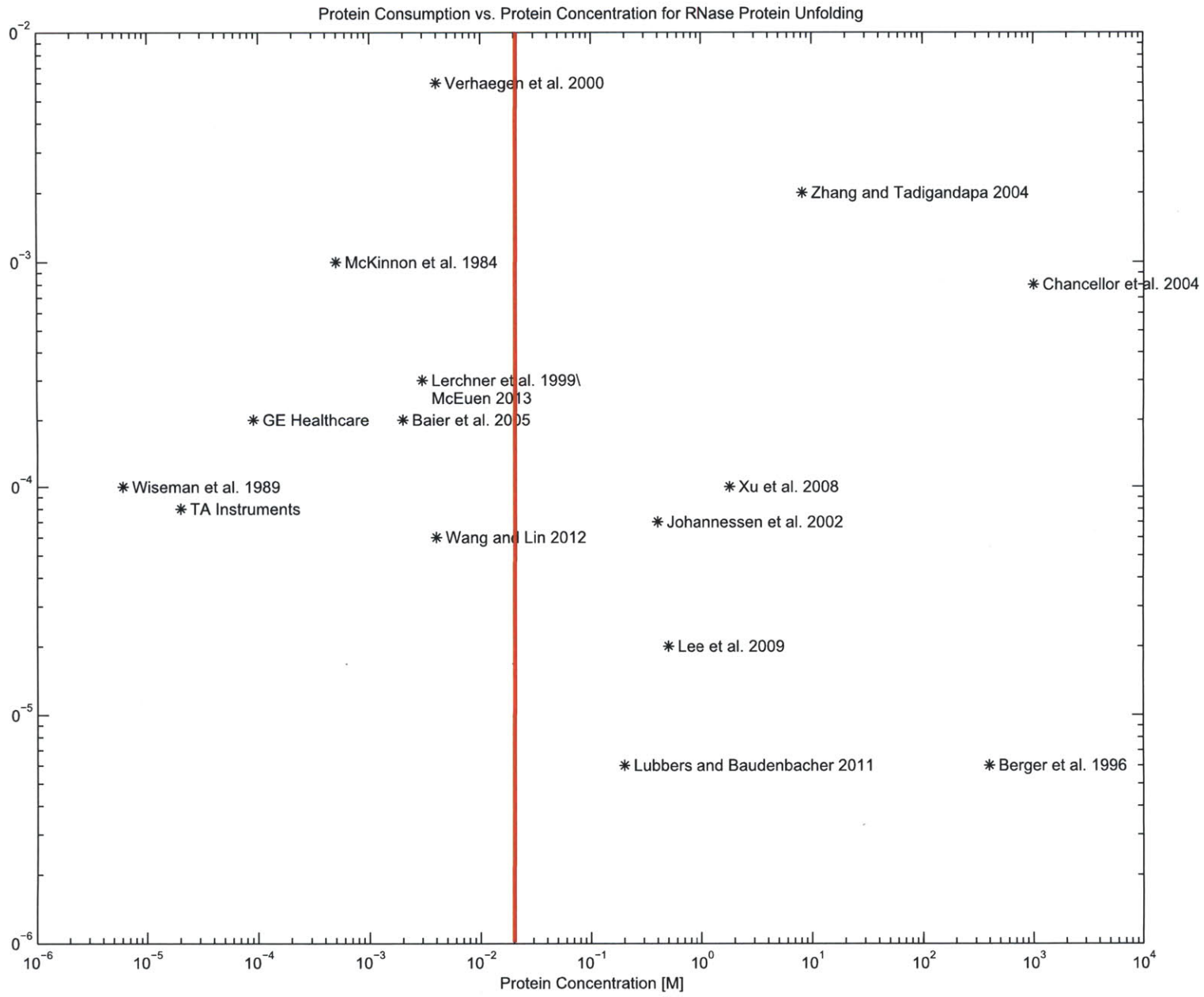

Figure 1-5: Life-sciences focused calorimeter literature survey: protein consumed vs. protein concentration.

Chapter 2

Calorimeter Design

This chapter documents the design and construction of a potentially disposable differential scanning calorimeter (DSC). The chapter is divided into the following sections to discuss the design and testing of the calorimeter.

- DSC System and Operation
- Cell Material Selection
- Fluid Handling
- Data Acquisition
- Calorimeter Design

Chapters 3 and 4 discuss calorimeter disturbance modeling and temperature control. These topics were separated from the present chapter so that they could be discussed in greater detail.

2.1 DSC System and Operation

First, to familiarize the reader with the calorimetric system, Figures 2-1 and 2-2 show its hardware and fluidic block diagrams. In addition, Table 2.1 contains details for each block in the hardware and fluidic block diagrams.

Table 2.1: Brief description of hardware used in block diagrams, Figures 2-1 and 2-2

Block Diagram Name	Hardware Part Number	Comments
Real-time PC	Speedgoat 4U ATX	MathWorks xPC target RTOS*
A/D	General Standards PMC-66-18AI32SSC1M-16-18B	16 channel 18-bit A/D
D/A	General Standards PMC66-18AO8	8 channel 18-bit D/A
Thermal actuator I amplifier	AE Techron LVC608	Low-noise linear amplifier
Temperature sensor I amplifier	Custom design	See Chapter 4
Temperature sensor II amplifier	EM Electronics A10	300 pV RMS, 1 second filter
Thermal actuator I	TE Technology CH-38-1.0-0.8	17 W circular peltier
Temperature sensor I	Heraeus 100485-4	Ni RTD 6720 ppm/^{0}C
Thermal actuator II	Vishay Y1625100R000Q9R	100 Ω 0.2 ppm/^{0}C 1206 resistor
Temperature sensor II	Thermix OTT-65-1.3-140	65 junction Bi_2Te_3 thermopile
Syringe pump	LabSmith SPS01	Programable 40 μL syringe pump
Valve	LabSmith AV201	3 port, 2 position rotary valve
Reference/sample cell	Custom design	See Section 2.5

*RTOS - real-time operating system

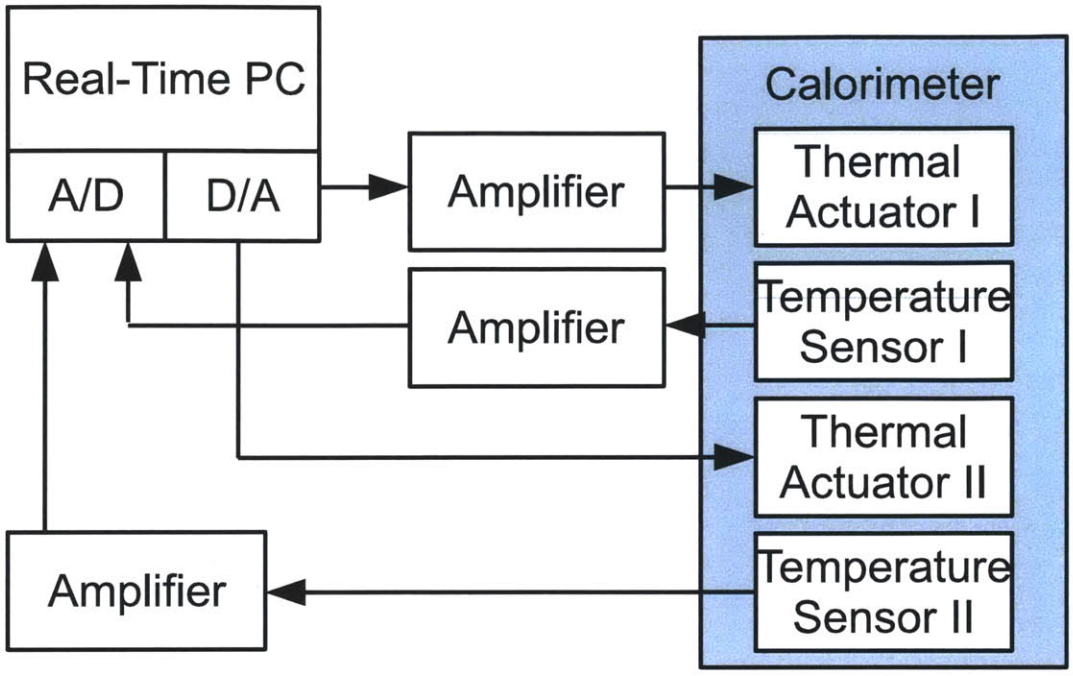

Figure 2-1: Calorimeter hardware block diagram.

The basic operation of any biochemical DSC includes four simple steps: 1) sample preparation, 2) sample loading, 3) temperature scan, and 4) data analysis. First a buffer solution is prepared for the reference cell, and a protein solution is prepared for the sample cell. It is important that the protein solution is prepared using the same buffer as that prepared for the reference cell because the purpose of the DSC is to measure the thermal events associated with the protein and not the thermal events from variation in the buffers. It is standard biochemical practice to prepare a buffer solution and then prepare the protein solution using buffer from the parent solution. When this is not possible, a biochemist may dialyze the solutions to ensure the buffers match. Lastly, it is common to degas the samples before loading them into the instrument.

Next the buffer solution is manually or automatically loaded into the reference cell. Likewise the protein solution is manually or automatically loaded into the sample cell. Although the majority of protein systems unfold well before 100^0C, this is not

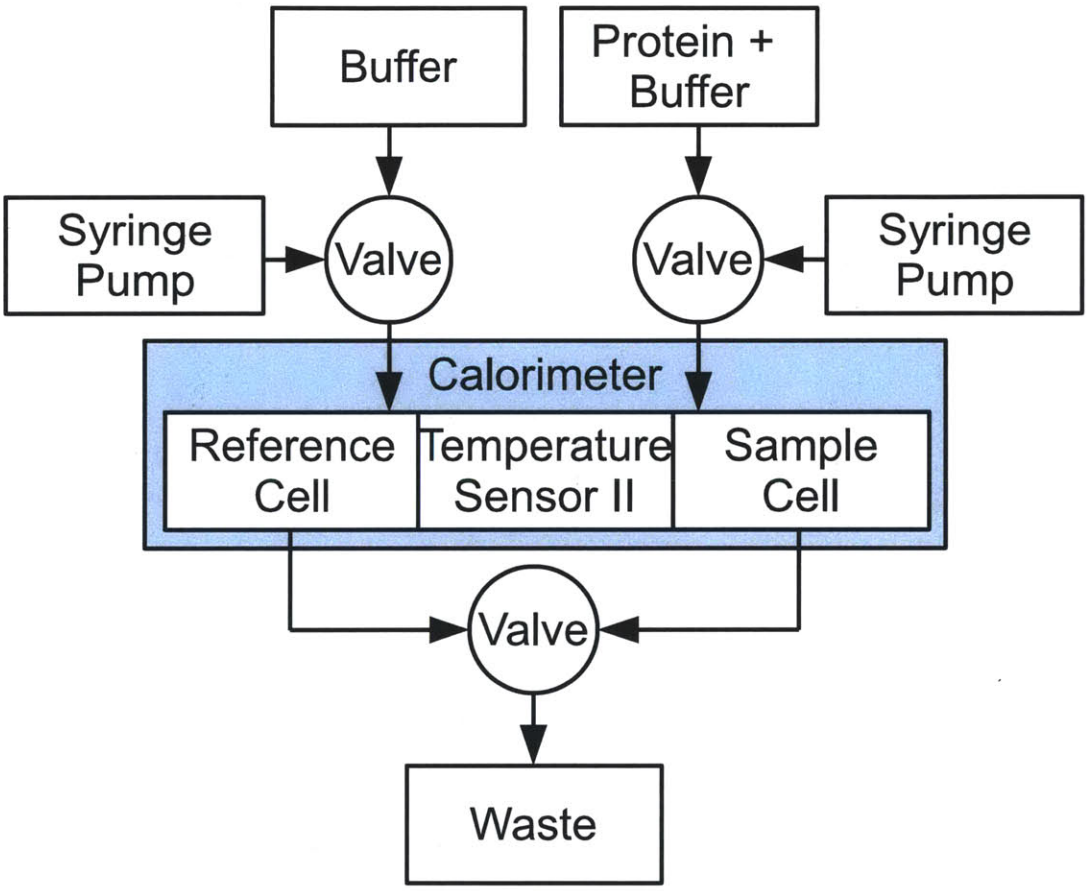

Figure 2-2: Calorimeter fluidic block diagram.

universally true. As a result, if the temperature scan range exceeds 100^0C, external pressure, typically through an external nitrogen tank, must be applied to the reference and sample cell. It is also common to perform a control experiment in which a buffer solution is loaded into both the reference and sample cell. The DSC of this study uses LabSmith hardware and software to automatically load samples (see Figure 2-2 and Table 2.1).

After the samples have been prepared and loaded, the instrument will cycle the reference and sample cells over the temperature range of interest. A thermal actuator, usually a peltier or resistive heater, heats the cells and a temperature sensor closes the feedback loop. A typical scanning range starts at 20^0C and stops at 80^0C, performed as a linear temperature ramp. Common scan rates span 50-200^0C/hr. While the instrument throughput could be increased through faster scan rates, there is evidence for some protein systems that at faster scan rates the protein unfolding kinetics can become rate limiting. In addition, depending on the nature of the transition, it is beneficial to scan slower to gain greater T_M temperature resolution, especially during a pre-formulation/formulation rank ordering study, as discussed in Chapter 1. The DSC of this study uses a single peltier device for heating and a Ni RTD for temperature feedback (see 2-1 and Table 2.1).

Finally after the experimental data is collected, it is analyzed. If a control experiment was performed, it is subtracted from the protein scan. Then a non-linear least squares fitting algorithm fits a thermodynamic model to the data. Over time various scientists have developed different thermodynamic models that describe protein unfolding [5]. However, since these models have already been well established and documented, this study does not explore them in detail.

Figure 2-3 displays a picture of the complete assembled calorimeter, including automated fluid handling. The LabSmith fluidic components are located on the left; there are three valves and two syringe pumps. The calorimeter is on the right and encased in a large block of rigid foam insulation. There is a black heat sink on top of the calorimeter that actively, via a fan, cools one side of the peltier device. Although difficult to see in the picture, there are borosillicate tubes that enter the calorimeter

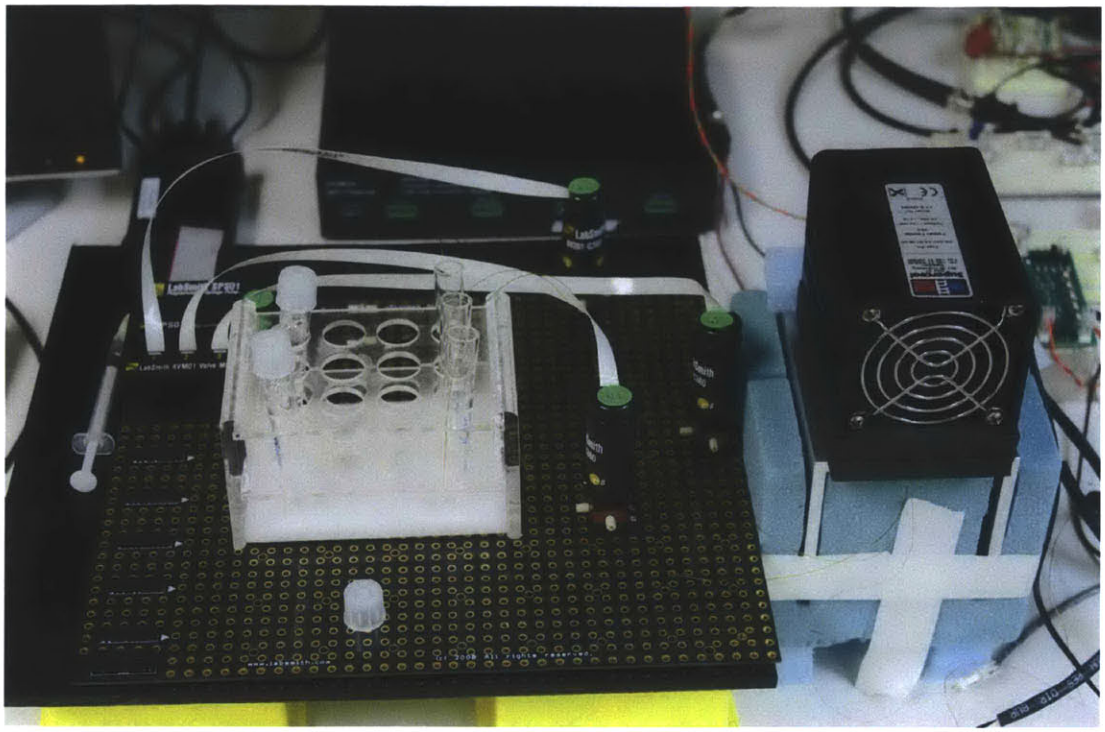

Figure 2-3: Picture of PhD Calorimeter setup.

below the black heat sink.

2.2 Cell Material Selection

With respect to the cell material selection for this calorimeter, there are two main requirements: 1) potential to be disposable and 2) bio-compatibility. Currently available commercial calorimeters (such as the VP Capillary DSC from GE Healthcare or the Nano DSC from TA Instruments) have non-disposable fixed cells, tantalum for the VP Capillary DSC and platinum for the Nano DSC. While there is a continual effort to design a consumable element into any instrument platform as an additional revenue source, in this case the driving force behind a disposable cell is technical and not commercial. Since a typical DSC experiment will scan a temperature range of 20-80^{0}C, an irreversible protein–which the majority of proteins are–will aggregate and clog the fluidic pathway of the device. In addition to the increased time needed to clean the cell, leftover aggregated protein can impact the data quality and bio-

chemistry of subsequent experimental runs. This may potentially lead to incorrect conclusions regarding the unfolding characteristics of said proteins.

There are several recent researchers who have developed sensitive calorimeters using MEMS fabrication techniques while citing disposability as a potential characteristic of their devices [17,30,34]. However, with current manufacturing technologies it would be difficult to produce and sell these devices for less than $10-20, which is about the maximum amount a single-use disposable would fetch in a typical biochemical lab. Currently there is one known company, Xensor Integration (http://www.xensor.nl), that markets a MEMS based calorimeter sensor device, which depending on the model, will cost roughly $150-250 per device. Since this price is indicative of the cost of a MEMS based calorimeter sensor, it would be cost prohibitive to make it disposable.

As a result, a significant aim of this work was to find a potential method to make a disposable calorimeter cell. Instead of using MEMS techniques and integrating all of the critical calorimeter sensor elements such as heaters, sensors, fluidics, and thermal isolation into a signal device, all these key elements were fixed except the microfluidic cell. Therefore, manufacturing techniques such as injection molding and hot embossing could be used to create an inexpensive microfluidic cell for pennies per cell. While the results of this thesis demonstrate that an unintegrated polymer microfluidic cell is capable of successfully performing DSC experiments, the technical challenges regarding how to repeatably use a disposable polymer microfluidic cell in a system were not the focus of this thesis. Thus polymer cells used for this thesis where attached to the thermopile with a conductive adhesive tape from 3M (part number 8805) and were not truly disposable. To the author's knowledge this is the only calorimeter approach that has the potential to create a disposable cell platform for less than $10-20 per cell.

The second important factor in cell material construction is bio-compatibility. It is critical that any material that comes in contact with protein solutions not biochemically alter the behavior of the biochemical system under study. Traditional material selections include various stainless steel alloys. More recently, however, polyether ether ketone (PEEK, an organic thermoplastic) and polyetherimides (PEI, also an or-

ganic thermoplastic) are becoming more common in biochemistry labs. While it was cost prohibitive to commission the tooling necessary to create injection molded parts out of PEEK or PEI for this study, the bio-compatibility of a readily available, high-temperature polycarbonate stereolithography resin analog, DSM Somos ProtoTherm 12120, was studies. As a result, monolithic microfluidic cells were designed and manufactured using stereolithography techniques. This allowed rapid design iteration and testing.

Since the purpose of this study did not include an in-depth biochemical study of protein unfolding but rather the design and construction of a disposable calorimeter, ribonuclease A (RNase A, Sigma Aldrich R5500) was chosen as the protein system to gauge bio-compatibility and performance testing. A 0.06 mM RNase A solution was prepared in a 50 mM potassium acetate buffer (KAc, Sigma Aldrich P-5708). Acetic acid (Sigma Aldrich A-0808) was added to the buffer until a pH of 5.5 was measured. These samples were prepared by the author's GE Healthcare colleague, Sheila Crofts.

Figures 2-4 and 2-5 show DSC scans of 0.06 mM RNase A with and without cured DSM Somos ProtoTherm 12120 shavings in a GE Healthcare VP Capillary DSC. While RNase A is one of the few known reversible proteins, it is not 100 percent reversible. After each rescan, the signal generated by the protein unfolding event became slightly smaller because of this irreversibility. Furthermore, both figures show the same results: the size, shape, and location of the unfolding peak does not change for both cases. Figure 2-4 does show some additional noise in the scans compared to Figure 2-5. However, this is a known artifact and is due to particles being present in the solution and not from any biochemical interaction. As a result, this data demonstrates that there is not any detrimental effects between RNase A and cured DSM Somos ProtoTherm 12120. Therefore, all polymer cells built in this study were made from cured DSM Somos ProtoTherm 12120.

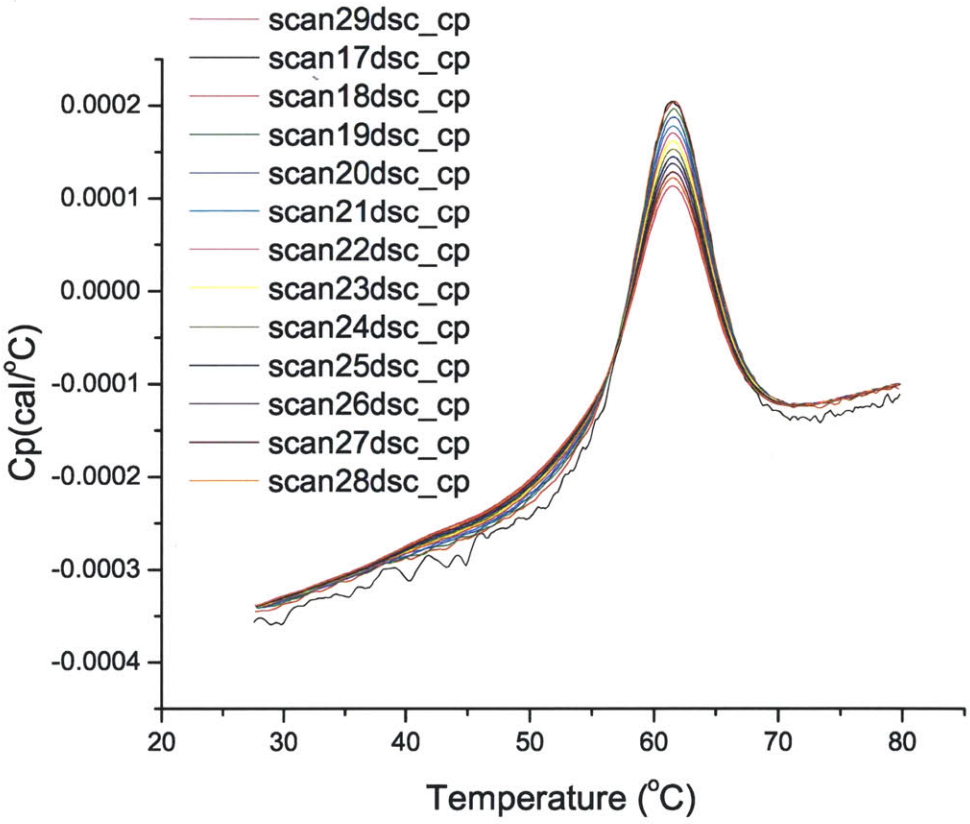

Figure 2-4: Thirteen scans of RNase A protein and DSM Somos ProtoTherm 12120 shavings in a GE Healthcare VP Capillary DSC.

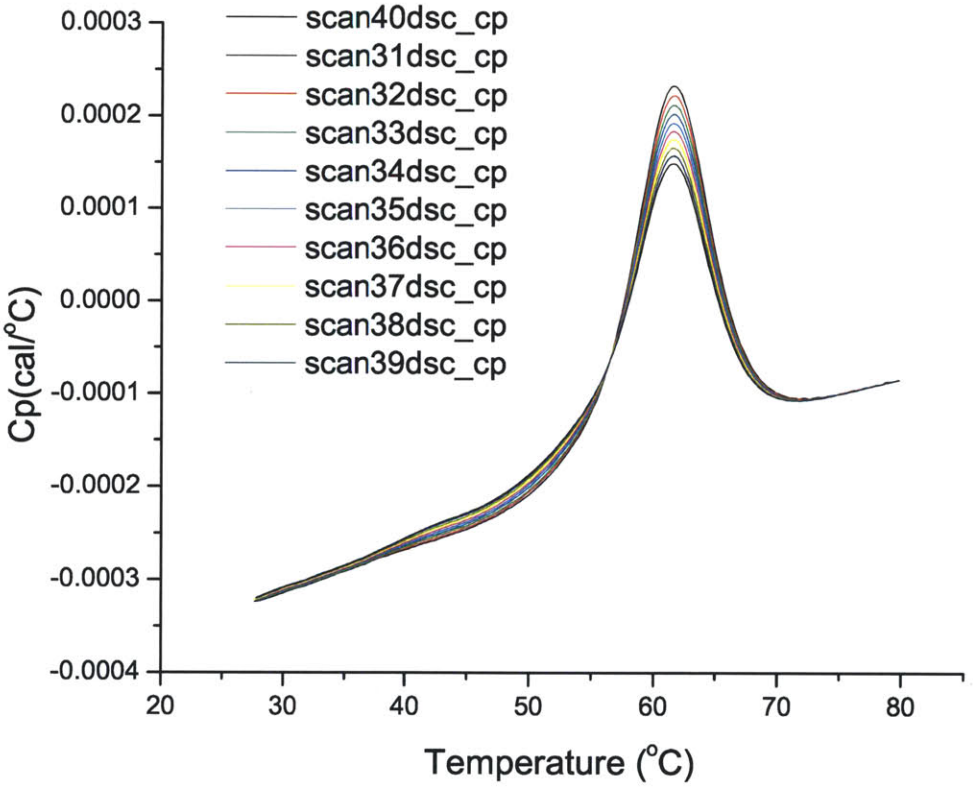

Figure 2-5: Ten scans of RNase A protein in GE Healthcare VP Capillary DSC.

2.3 Fluid Handling

Protein consumption, as discussed in Chapter 1, is one of the most important requirements of a biochemical calorimeter. The fluid handling platform for this study was carefully considered to minimize the loss of precious protein sample as fluidic dead volume, sample that is not needed for the experiment. Many research calorimeter designs fail to adequately address fluid handling. For example, there are several researchers who have designed calorimeters with cell volumes less than 5 nL [7, 8, 17, 20, 40, 41]. However, since calorimeter data is highly dependent on concentration, how does one effectively integrate these sub 5 nL devices with academic, biotech, and pharma compounds and compound libraries without significantly impacting the concentration due to evaporation? It is difficult to do so, unless the dead volumes are large, potentially hundreds of nanoliters. As a result, a key driver for a small volume cell, protein consumption, is lost due to the large dead volume needed to interact with the device.

The cell volume of this device, 10 μL, was specifically chosen such that the fluidic dead volume would be a fraction of the total volume. As detailed in Figure 2-2 and Table 2.1 all fluidic handling components were purchased from LabSmith. The LabSmith hardware was controlled by a simple custom script generated within their software. Figure 2-6 shows an image of the LabSmith software and custom script. In addition, 360 μm OD $\times$ 100 μm ID borosilicate capillary tubing connected all of the valves, syringe pumps, and cells. The total dead volume of the current prototype setup is approximately 5 μL, where 4 μL are from the capillary tubing and 1 μL is from the combined dead volume of all three valves. With a more refined design, it should be possible to reduce the total dead volume to less than 2 μL. 12 μ per experiment is approximately 30-40 times less than commercially available instruments with respect to the total amount of sample required for a single experiment. However, this calorimeter is not as sensitive as these commercially available devices and so the lower volume is only of benefit for high concentration studies such as those performed in pre-formulation and formulation development as discussed in Chapter 1.

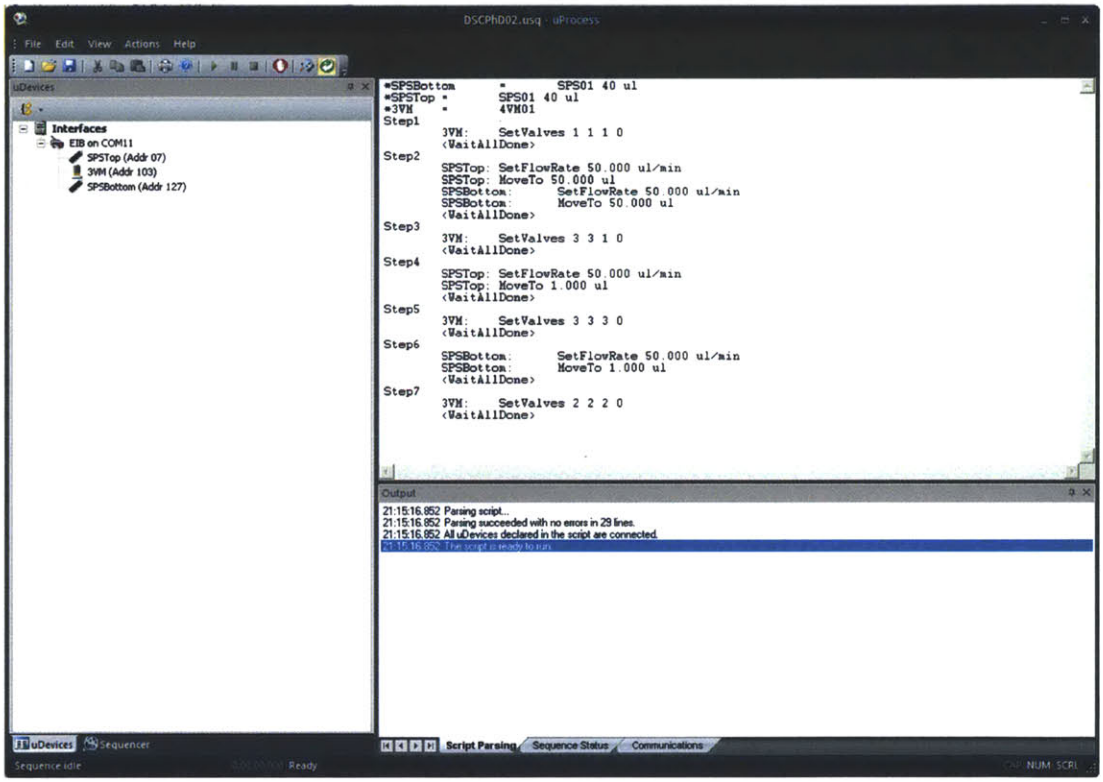

Figure 2-6: LabSmith custom script that drives the syringe pumps and valves to automatically load the calorimeter.

2.4 Data Acquisition

Figure 2-7 displays a frequency domain comparison of several different data acquisition strategies. The Institute of Electrical and Electronics Engineers (IEEE) Standards 1057, *IEEE Standard for Digitizing Waveform Recorders*, and 1241, *IEEE Standards for for Terminology and Test Methods for Analog-to-Digital Converters*, document several testing procedures to experimentally determine the dynamic range of an analog-to-digital data acquisition system [2,3]. The recommended testing protocol in IEEE Standard 1241 was followed. See Chapter 4, Figure 5 of the standard, to compare the noise performance of four different data acquisition strategies: 1) an Agilent 34792A unit with an integration period of two power line cycles (PLC), 2) a Data Translation DT9824 unit (24 bit delta-sigma A/D converters), 3) an 18-bit General Standards (labeled as Speedgoat in Figure 2-7) PMC-66-18AI32SSC1M-16-18B card sampled at 10 Hz, and 4) an 18-bit General Standards PMC-66-18AI32SSC1M-16-18B card sampled at 40 kHz averaged (using a simple unweighted FIR filter) and decimated to 10 Hz [3]. A 16-bit Agilent 33220A function generator was used to generate a 50 mHz 9.95 V sine wave as the input to each of the four systems. It should be noted that as recommended by the IEEE 1241 standard, a simple RC filter ($f = \frac{1}{2\pi RC} = 1$ Hz) was inserted between the function generator and the data acquisition system to more accurately quantify the noise of the data acquisition system below the noise threshold of the sine wave source. Finally, to generate Figure 2-7 a fast fourier transform (FFT) was calculated for 1024 points for each system using a Hanning window.

A number of important observations can be made regarding the four different data acquisition systems displayed in Figure 2-7. First, the apparent resonant peaks of the Agilent 34972A setup are not an artifact. The test was run at a different sampling frequency and similar peaks were present. The source of the peaks is unknown. Second, an oversampled and averaged 18-bit successive approximation register (SAR) data acquisition system is capable of nearly achieving the performance of a 24-bit delta sigma data acquisition system. Both show more than six orders of magnitude of

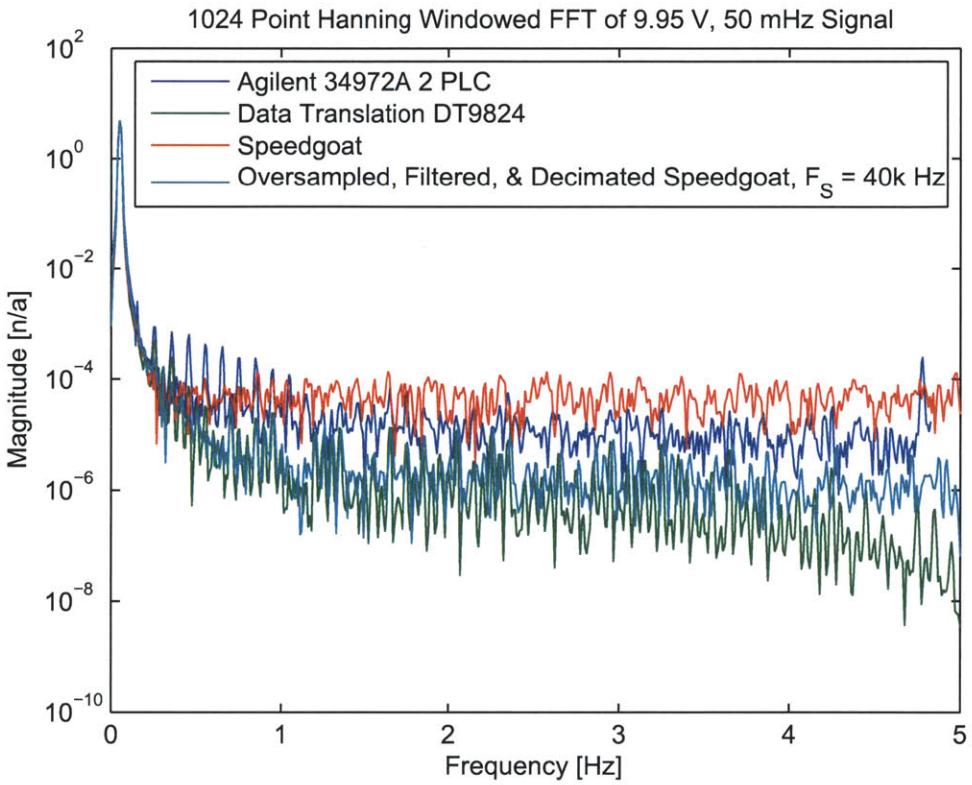

Figure 2-7: A comparison of different data acquisition strategies.

separation between the input 50 mHz 9.95 V sinusoidal waveform and the respective data acquisition noise floor. This is equivalent to more than 20 bits of noise free performance. Finally, while the DT9824 system was the most sensitive, the oversampled and averaged 18-bit system was chosen for convenience. Speedgoat is a Swiss company that provides a real-time data acquisition environment that seamlessly integrates with MATLAB and Simulink products from MathWorks. As a result, it was faster to develop and perform real-time digital control loops with Speedgoat hardware (i.e., 18 bit A/D and D/A boards described in Table 2.1). Except for the development of a temperature control circuit, as described in Chapter 4, an oversampled and averaged Speedgoat data acquisition system was used for the development and testing of this differential scanning calorimeter.

2.5 Calorimeter Design

Temperature measurement is ubiquitous. Table 2.2 contains various temperature measurement technologies and theoretical minimum sensitivities. The derivations of the temperature sensitivities for thermistors, thermopiles, and RTDs are straightforward and can be found in several sensor measurement texts. As was mentioned in Table 1.1, the majority of life sciences' specific calorimeters use thermopiles as the fundamental sensing technology. This is not surprising considering that from a fundamental temperature sensitivity limit, thermopiles are the second most sensitive device in the table. A 65 junction bismuth-telluride, Bi_2Te_3, thermopile was chosen from Thermix Ltd. as the sensing technology for this calorimeter.

While a liquid expansion technique shows more potential sensitivity, it would be difficult to use in a scanning instrument. In order to increase the sensitivity of a liquid expansion device the diameter of the fluid filled vessel must be small, 10-100s of microns. David and Hunter built a liquid expansion calorimeter that achieved a temperature sensitivity of 1 μ^0C [9]. It should be noted that this device was setup in an absolute, not differential manner. As a result, more than eight orders of magnitude (1 μ^0C-100^{0}C) of dynamic range would be necessary for this sensor technology to be

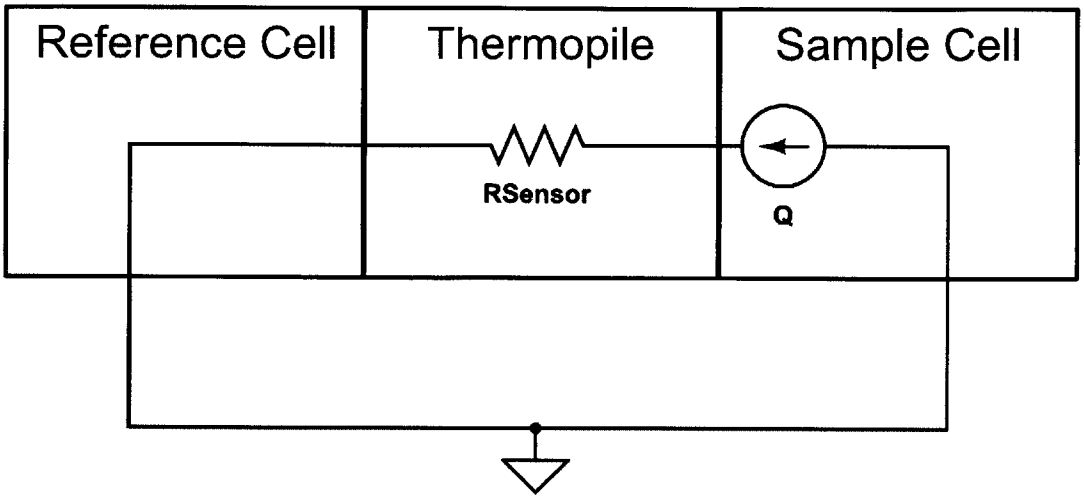

Figure 2-8: Simple steady-state heat transfer calorimeter model.

used in a scanning calorimeter. Such a large dynamic range could be achieved with an interferometer as was used in the published work. Unfortunately, in order to measure the liquid expansion, a microscope objective lens was used to focus the laser interferometer beam on the fluid meniscus. As a result, the working distance of the objective lens chosen limits the dynamic range of the measurement considerably, roughly 1 nm - 1 mm or six orders of magnitude. Therefore, with a similar setup, it would not be possible to build a scanning calorimeter with this technique. However, if a differential liquid expansion setup could be designed such that the dynamic range is no longer limiting, a liquid expansion sensing technology could show tremendous promise in future calorimeter designs.

After a thermopile sensor was chosen, a model was created to estimate the performance of a thermopile based calorimeter. There are a number of examples of calorimeter models that describe the equations that govern the performance of a thermopile based calorimeter [12, 34, 37]. The following derivation pulls ideas from the cited papers above. Figure 2-8 shows a simple model of the performance of a thermopile based calorimeter.

Equation 2.1 demonstrates how to calculate the temperature gradient produced by a protein unfolding event.

Table 2.2: Brief description of common temperature sensing technologies and theoretical minimum sensitivities.

Technology	Theoretical Sensitivity [^{0}C]	Fundamental Physics
Thermistor	9×10^{-7}	$T_{\text{Noise}} = \frac{2R\sqrt{4k_BTR\Delta f}}{\left(\frac{dR}{dT}\right)v_S}$
Thermopile	4×10^{-8}	$T_{\text{Noise}} = \frac{\sqrt{4k_BTR_{\text{TP}}\Delta f}}{nS}$
RTD	4×10^{-6}	$T_{\text{Noise}} = \frac{\sqrt{4k_BTR_{\text{RTD}}\Delta f}}{\left(\frac{dR_{\text{RTD}}}{dT}\right)i_{\text{Test}}}$
Liquid expansion	7×10^{-10}	$T_{\text{Noise}} = \frac{\pi D^2\Delta L}{4\alpha_V V}$ [9]
Bimetallic	1×10^{-5}	$T_{\text{Noise}} = \frac{2\delta\left(E_A^2t_A^4+4E_AE_Bt_A^3t_B+6E_AE_Bt_A^2t_B^2+4E_AE_Bt_At_B^2+E_B^2t_B^4\right)}{(x^2+\delta^2)[6E_AE_Bt_At_B(t_A+t_B)(\alpha_A-\alpha_B)]}$ [11]
IC Thermometer	1×10^{-7}	see p. 11-48 in [23]
Quartz Thermometer	1×10^{-4}-1×10^{-6}	[29]

$$\Delta T = \dot{Q} R_{\text{Sen}} \tag{2.1}$$

where ΔT is the temperature gradient across the cells measured by the thermopile, $\dot{Q}$ is the power produced by the protein unfolding, $R_{\text{Sen}} = \frac{L}{kA}$ is the thermal resistance of the thermopile sensor, L is the distance through which heat flows, k is the thermal conductivity of the material, and A is the cross sectional through which heat flows.

This simplistic equation assumes that the thermal resistance of the thermopile sensor is much less than any other thermal resistance (i.e., thermal pathway) to the outside world. Examples of other thermal pathways include: electrical leads for resistive heaters that are attached to the cell, fluidic connections to the cells, and any other conductive, convective, or radiative heat transfer pathway. To a limited degree the designer has control over these additional thermal pathways and materials and geometries can be chosen such that this assumption holds. For example, Lee et al. used a mechanical vacuum pump in their calorimeter design to increase the thermal resistance of a convective heat transfer pathway to ensure that the heat from the experiment passed through the thermopile sensor [17].

Equation 2.2 links the temperature gradient across a thermopile to the self-generated voltage of the thermopile as modeled by the Seebeck effect. It should be noted that it includes a theoretical sensitivity limit due to Johnson noise of the thermopile.

$$\Delta V = nS\Delta T + \sqrt{4k_B T R_{\text{Elec}} \Delta f} \tag{2.2}$$

where ΔV is the self-generated thermopile voltage, n is the number of thermocouple junctions, S is the combined Seebeck coefficient of the material pair used in the thermopile, k_B is Boltzman's constant, T is the absolute temperature of the device, R_{Elec} is the electrical impedance of the thermopile, and Δf is the bandwidth of the measurement.

Equation 2.4 combines Equations 2.1 and 2.2 and solves for the minimum detectable power $\dot{Q}_{\text{Min}}$.

$$\dot{Q}_{Min} = \frac{\sqrt{4k_BTR_{\text{Elec}}\Delta f}}{nS\left(\frac{L}{kA}\right)} \tag{2.3}$$

$$= \frac{kA\sqrt{4k_BTR_{\text{Elec}}\Delta f}}{nSL} \tag{2.4}$$

From a calorimeter design perspective, the goal should be to minimize $\dot{Q}_{\text{Min}}$. However, it is important first to note that k_B, T, and Δf are essentially constant. Boltzman's constant, k_B, is a measured value and cannot be changed by the designer. The absolute temperature, T, is constrained by the calorimetry application; protein characterizing calorimeters perform measurements in the maximum temperature range of 10-150^{0}C. As mentioned previously, however, most experiments are performed between 20-80^{0}C. Finally, the measurement bandwidth is determined by the scan rate used in the experiment. Because of studies that have shown protein unfolding kinetic limitations above 200^{0}C/hr, a typical experiment may last between 30-60 minutes, which is basically 0 Hz or DC. The upper limit is 1 Hz since protein transitions occur over tens of seconds for fast protein unfolding transitions. As a result, the measurement bandwidth is 1 Hz (i.e., $\Delta f = f_2 - f_1 = 1\text{Hz} - 0\text{Hz} = 1\text{Hz}$)

Therefore the designer has k, A, R_{Elec}, n, S, and L left to minimize Equation 2.4. As mentioned in Section 2.2, this calorimeter design is intentionally separating the microfluidic cells from the rest of the device and is not using MEMS techniques to fabricate the device. As a result, while other researchers have had a great deal of latitude in impacting the thermopile parameters above, this thesis was constrained by the need to find an off-the-shelf thermopile sensor that minimized $\dot{Q}_{\text{Min}}$ [14,17,19, 33,34,40]. The Thermix Ltd. Bi_2Te_3 thermopile sensor was chosen to minimize $\dot{Q}_{\text{Min}}$.

Table 2.3 contains values used in this thesis for the parameters in Equation 2.4. Compared to previous measured values (see Table 1.1), this calculated value of 1.9 nW seems reasonable. Furthermore, for isothermal titration calorimeters (ITC) where the experiments are performed at a constant temperature, this limit is starting to become limiting [17]. However, for scanning calorimeters the author has not found any evidence in the literature of a thermopile based calorimeter that is within one

order of magnitude of this fundamental limit. This may be due to the dynamic nature of performing a calorimetric experiment while ramping temperature. In addition, those papers that discuss a measured power sensitivity close to the the theoretical limit performed the experiment while thermostating at a constant temperature and not during a temperature ramp. The device described in this thesis demonstrates the same behavior: the calibrated short-term power noise is significantly less while thermostating then during a scanning experiment.

Table 2.3: Realistic parameter values for Equation 2.4

Parameter	Value	Units
k	1.2	W/m-K
A	30×10^{-6}	m^2
k_B	1.38×10^{-23}	m^2kg/s^2-K
T	350	K
R_{Elec}	24	Ω
Δf	1	Hz
n	64	n/a
S	200×10^{-6}	$V/^0C$
L	1×10^{-3}	m
$\dot{Q}_{Min}$	1.9	nW

As a result, since the thermopile sensor is not sensitivity limiting in a scanning calorimeter, the major aim of this thesis, in addition to designing a disposable calorimeter, is to understand how to minimize the impact of outside disturbances on the measurement of protein unfolding. Chapters 3 and 4 detail how to model the influence of these outside disturbances and how to improve the noise on the temperature ramp.

Chapter 3

Modeling

3.1 Analytic Heat Transfer Model

Figure 3-1 contains an abstract transient heat transfer model to capture the transfer function between the calorimeter base temperature and the temperature measured across the thermopile sensor. Note that C_i refer to thermal capacitors R_i refer to thermal resistors, and T_i refer to temperatures. Although in this simplified model, the thermal capacitors of both cells are assumed to be equivalent, their transient behavior is independent of one another. As a result, there are three independent energy storage elements in this model: 1) the sample cell thermal capacity - C_1, 2) the reference cell thermal capacity - C_1, and 3) the thermal capacity of the thermopile sensor - C_2.

Figure 3-2 contains a labeled circuit model; the Qi terms are heat fluxes. Equations 3.1-3.3 contain the governing differential equation for each independent energy storage element.

$$\dot{Q}_2 = C_1 \frac{dT_{\mathrm{R}}}{dt} \tag{3.1}$$

$$\dot{Q}_5 = C_1 \frac{dT_{\mathrm{S}}}{dt} \tag{3.2}$$

$$\dot{Q}_7 = C_2 \frac{dT_{\mathrm{T}}}{dt} \tag{3.3}$$

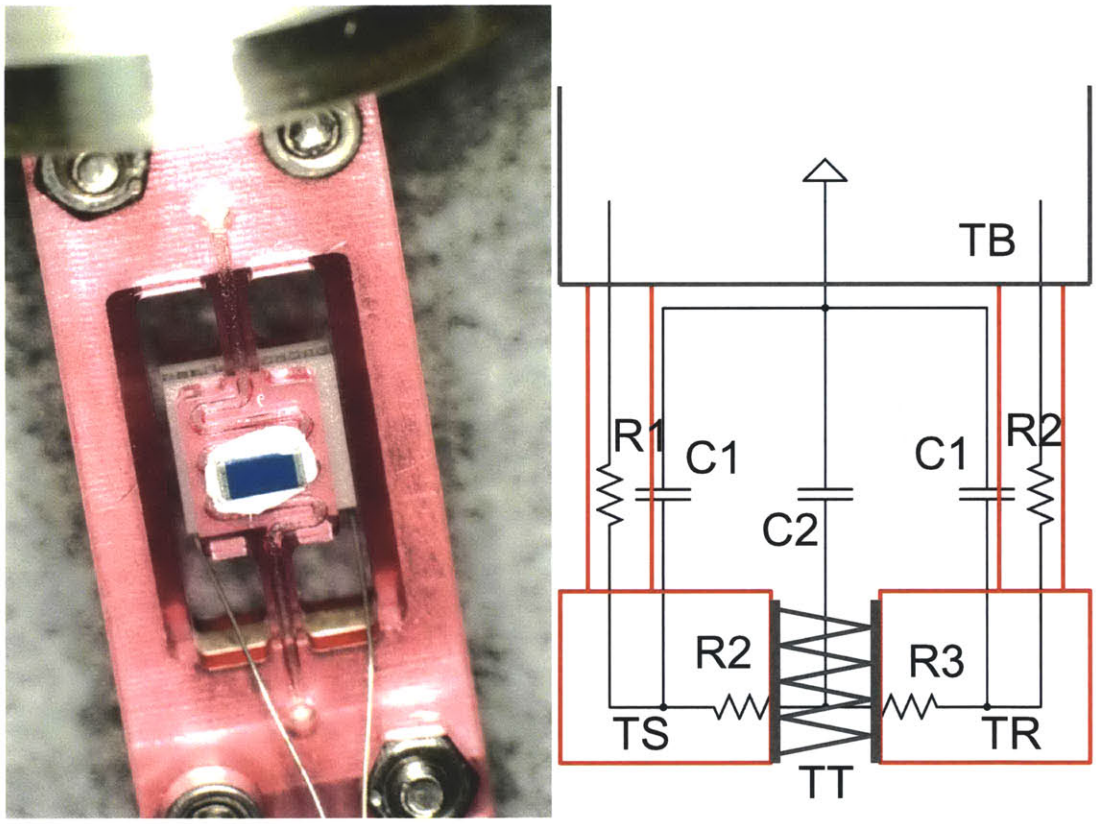

Figure 3-1: Transient heat transfer model abstraction from calorimeter hardware.

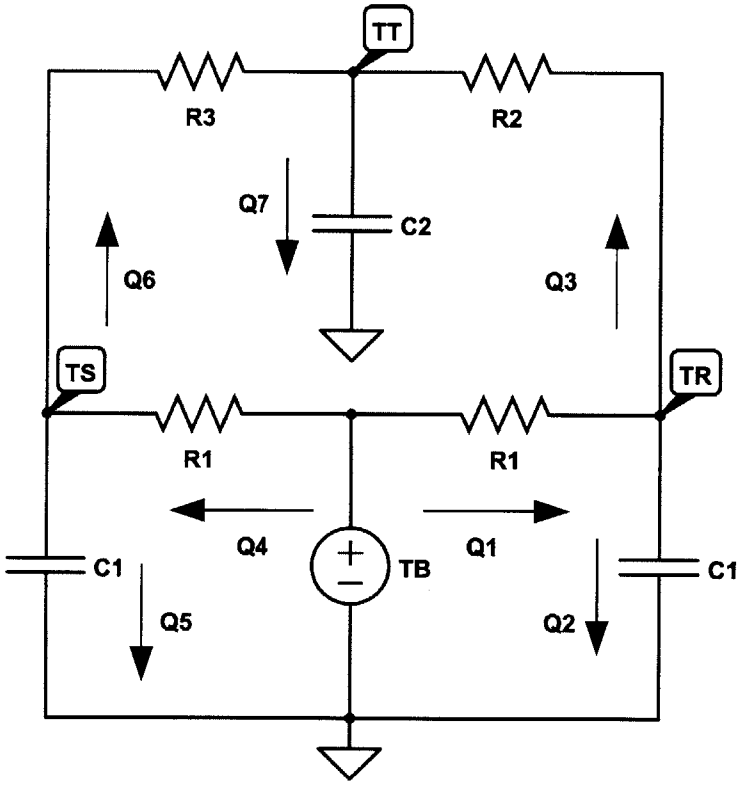

Figure 3-2: Transient heat transfer network model for the calorimeter.

where the subscripts R, S, T, and B refer to reference cell, sample cell, thermopile, and base.

Use the thermal equivalent of Kirkoff's voltage law and Ohm's law to simplify Equations 3.1-3.3.

$$\frac{dT_{\mathrm{R}}}{dt} = \frac{1}{C_1}\left[-\left(\frac{1}{R_1}+\frac{1}{R_2}\right)T_{\mathrm{R}} + \frac{1}{R_2}T_{\mathrm{T}} + \frac{1}{R_1}T_{\mathrm{B}}\right] \tag{3.4}$$

$$\frac{dT_{\mathrm{S}}}{dt} = \frac{1}{C_1}\left[-\left(\frac{1}{R_1}+\frac{1}{R_3}\right)T_{\mathrm{S}} + \frac{1}{R_3}T_{\mathrm{T}} + \frac{1}{R_1}T_{\mathrm{B}}\right] \tag{3.5}$$

$$\frac{dT_{\mathrm{T}}}{dt} = \frac{1}{C_2}\left[\frac{1}{R_2}T_{\mathrm{R}} + \frac{1}{R_3}T_{\mathrm{S}} - \left(\frac{1}{R_2}+\frac{1}{R_3}\right)T_{\mathrm{T}}\right] \tag{3.6}$$

Now take Equations 3.4-3.6 and put into state-space form. Note that the desired output is the difference between the reference and sample cell temperatures, $y = T_{\mathrm{R}} - T_{\mathrm{S}}$, since this represents the temperature measured and subsequently amplified by the thermopile temperature sensor.

$$\frac{d}{dt}\begin{bmatrix} T_{\mathrm{R}} \\ T_{\mathrm{S}} \\ T_{\mathrm{T}} \end{bmatrix} = \begin{bmatrix} \frac{-1}{C_1}\left(\frac{1}{R_1}+\frac{1}{R_2}\right) & 0 & \frac{1}{R_2C_1} \\ 0 & \frac{-1}{C_1}\left(\frac{1}{R_1}+\frac{1}{R_3}\right) & \frac{1}{R_3C_1} \\ \frac{1}{R_2C_2} & \frac{1}{R_3C_2} & \frac{-1}{C_2}\left(\frac{1}{R2}+\frac{1}{R_3}\right) \end{bmatrix}\begin{bmatrix} T_{\mathrm{R}} \\ T_{\mathrm{S}} \\ T_{\mathrm{T}} \end{bmatrix} + \begin{bmatrix} \frac{1}{R_1C_1} \\ \frac{1}{R_1C_1} \\ 0 \end{bmatrix} T_{\mathrm{B}}$$

$$y = \begin{bmatrix} 1 & -1 & 0 \end{bmatrix}\begin{bmatrix} T_{\mathrm{R}} \\ T_{\mathrm{S}} \\ T_{\mathrm{T}} \end{bmatrix} + \begin{bmatrix} 0 \end{bmatrix} T_{\mathrm{B}}$$

In order to fit an experimental model to this system, the state-space form must be converted into a continuous transfer function in the Laplace domain. Equation 3.7 displays the transfer function using the common state-space to transfer function formula: $H(s) = \mathbf{C}\left(s\mathbf{I} - \mathbf{A}\right)^{-1}\mathbf{B} + \mathbf{D}$, where $\mathbf{A}$, $\mathbf{B}$, $\mathbf{C}$, and $\mathbf{D}$ are the state-space matrices and $\mathbf{I}$ is the identity matrix.

$$H(s) = \frac{as}{s^3 + ks^2 + ls + m} \tag{3.7}$$

$$a = \left(\frac{C_2R_1R_2 - C_2R_1R_3}{C_1^2C_2R_1^2R_2R_3}\right) \tag{3.8}$$

$$k = \left(\frac{C_1^2R_1^2R_2 + C_1^2R_1^2R_3 + C_1C_2R_1^2R_2 + C_1C_2R_1^2R_3 + 2C_1C_2R_1R_2R_3}{C_1^2C_2R_1^2R_2R_3}\right) \tag{3.9}$$

$$l = \left(\frac{2c_1R_1 + C_2R_1^2 + 2C_1R_1R_2 + 2C_1R_1R_3 + C_2R_2R_3}{C_1^2C_2R_1^2R_2R_3}\right) \tag{3.10}$$

$$m = \left(\frac{2R_1 + R_2 + R_3}{C_1^2C_2R_1^2R_2R_3}\right) \tag{3.11}$$

$$\tag{3.12}$$

This transfer function displays an interesting mathematical property. The formula shows that if $R_2 = R_3$, the calorimeter will fully attenuate any disturbances from the base. Although not the topic of this thesis, part of the future work should be to investigate what strategies can be used to ensure that R_2 and R_3 are as close to each other as possible.

In order to fit experimental data to this model, the inverse laplace of Equation 3.7 must be calculated. However, before proceeding knowledge regarding thermal dynamic systems can be applied to simplify the potential mathematical cases for this function. Unlike mechanical, electrical, and fluidic systems, there is no equivalent inertial term in thermal systems. As a result, in an open loop thermal system resonance cannot physically happen. In order for resonance to occur in a dynamic system there must be both an inertial term and potential energy storage term. Therefore, the transfer function in Equation 3.7 can be rewritten to factor the denominator into real roots (i.e., resonance leads to complex roots). Equations 3.13-3.15 show the new generic transfer function in the Laplace domain and the impulse response in the time domain.

$$H(s) = \frac{as}{(s+b)(s+c)(s+d)} \tag{3.13}$$

$$h(t) = \mathcal{L}^{-1}\{H(s)\} \tag{3.14}$$

$$= a\left(-\frac{be^{-bt}}{(b-c)(b-d)} + \frac{ce^{-ct}}{(b-c)(c-d)} + \frac{de^{-dt}}{(b-d)(d-c)}\right) \tag{3.15}$$

where b, c, and d are real roots of the cubic polynomial in the denominator of the transfer function.

With the derivation of an analytic heat transfer model, it is important to create an experiment to verify the validity of said model. The next section describes a linear stochastic test that was used to measure the impulse response function of the calorimeter.

3.2 Linear Stochastic System Identification

There are several experimental methods to experimentally identify a dynamic system. Linear stochastic system identification is one method that can be used to identify a dynamic system. Figure 3-3 displays the experimental setup of the stochastic test used for this calorimeter. A hard-limited stochastic signal was applied to the peltier device, and the nickel RTD temperature and thermopile voltage were measured. The thermopile voltage was converted to a temperature gradient across the thermopile using Equation 3.16. The experiment was run for 5000 seconds.

$$\Delta T = \frac{V}{nSG} \tag{3.16}$$

where ΔT is the temperature gradient across the thermopile, V is the amplified thermopile voltage, n is the number of thermopile junctions, S is the thermopile Seebeck coefficient, and G is the gain of the electronic thermopile amplifier.

The model in Figure 3-1 and Equation 3.15 shows the relationship between temperature base input, Ni RTD, and thermopile output. As a result, when the impulse response was calculated the Ni RTD signal was treated as the input (as opposed

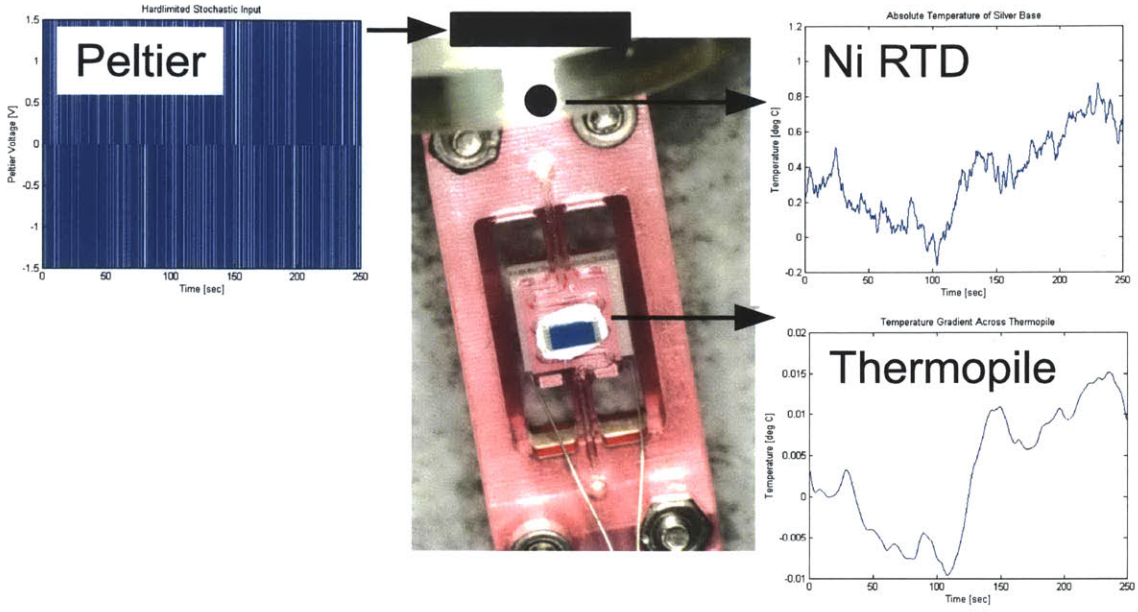

Figure 3-3: Linear stochastic system identification of calorimeter.

to the hard-limited peltier voltage input) and the thermopile voltage as the output. The impulse response of this input output relationship was calculated using notes from Professor Ian Hunter's MIT 2.131 Spring 2009 course notes [13]. Equation 3.17 calculates the impulse response function.

$$h_{\text{Est}} = F_S \left(\mathbf{C}_{xx}^{-1} c_{xy} \right) \tag{3.17}$$

where h_{Est} is the calculated impulse response function, F_S is the sampling frequency, $\mathbf{C}_{xx}^{-1}$ is the inverse of a Toeplitz matrix of the input auto-correlation function, and c_{xy} is the input-output cross-correlation function.

Now that a model has been created and a test to verify the model has been determined, the final section will discuss the non-linear least squares fit to the experimental data.

3.3 Non-Linear Least Squares Fitting

In order to verify the quality of the analytic model described in Section 3.1, it is critical to fit the model against experimental data and compare it with calculated values. Equations 3.18-3.20 show expressions for conductive and convective thermal resistances and thermal capacitance.

$$R_{\text{Conduction}} = \frac{L}{kA_{\text{Conduction}}} \tag{3.18}$$

$$R_{\text{Convection}} = \frac{1}{hA_{\text{Convection}}} \tag{3.19}$$

$$C_{\text{Thermal}} = \rho V C_P \tag{3.20}$$

where $R_{\text{Conduction}}$ is the conductive thermal resistance, $R_{\text{Convection}}$ is the convective thermal resistance, C_{Thermal} is the thermal capacitance, L is the thickness through which heat flows, k is is the thermal conductivity, $A_{\text{Conduction}}$ is the cross-sectional area through which heat flows, h is the convective coefficient, $A_{\text{Convection}}$ is the surface area through which convective heat flows, ρ is the density of the material, V is the volume of the material, and C_P is the specific heat of the material.

Table 3.1 contains material and geometric properties of the calorimeter in question. Many of these values are reported as ranges because those are values that are reported by material manufacturers. Other then the geometric properties, which have been verified by direct measurement, the material properties have not been directly measured.

Equations 3.21-3.25 contain specific expressions for the calculation of the relevant thermal resistors and capacitors of the PhD calorimeter.

Table 3.1: Geometric and material properties of PhD Calorimeter.

Parameter	Value	Units
ρ_{Water}	1000	kg/m^3
ρ_{Polymer}	1150	kg/m^3
ρ_{BiTe}	7700	kg/m^3
ρ_{AlO}	3950	kg/m^3
$C_{\text{P,Water}}$	4180	J/kg-K
$C_{\text{P,Polymer}}$	1200-2100	J/kg-K
$C_{\text{P,BiTe}}$	154-544	J/kg-K
$C_{\text{P,AlO}}$	837-880	J/kg-K
k_{Polymer}	0.1-0.7	W/m-K
k_{TIM}	0.6	W/m-K
h	5-25	$\text{W/m}^2\text{-K}$
V_{Water}	10e-9	W/m-K
V_{Polymer}	26e-9	W/m-K
V_{BiTe}	26e-9	W/m-K
V_{AlO}	26e-9	W/m-K
$A_{\text{Convection}}$	1.1e-3	m^2
A_{Polymer}	30e-6	m^2
A_{TIM}	30e-6	m^2
L_{TIM}	125e-6	m
L_{Polymer}	1.2e-3	m
$R_{\text{Thermopile}}$	100	K/W

$$C_1 = \rho_{\text{Water}} V_{\text{Water}} C_{\text{P,Water}} + \rho_{\text{Polymer}} V_{\text{Polymer}} C_{\text{P,Polymer}} \tag{3.21}$$

$$C_2 = \rho_{\text{BiTe}} V_{\text{BiTe}} C_{\text{P,BiTe}} + \rho_{\text{AlO}} V_{\text{AlO}} C_{\text{P,AlO}} \tag{3.22}$$

$$R_1 = \frac{1}{hA_{\text{Convection}}} \tag{3.23}$$

$$R_2 = \frac{R_{\text{Thermopile}}}{2} + \frac{L_{\text{TIM}}}{k_{\text{TIM}} A_{\text{TIM}}} + \frac{L_{\text{Polymer}}}{k_{\text{Polymer}} A_{\text{Polymer}}} \tag{3.24}$$

$$R_3 = R_2 \tag{3.25}$$

Figure 3-4 displays the estimated (non-parametric) impulse response, the fitted (parametric) impulse response, and the impulse response using the state-space model above with the fitted parameters. A non-linear least squares fitting algorithm was used to fit Equation 3.15 to the experimental data discussed in Section 3.2. One determination of the quality of fit is known as the variance-accounted-for (VAF). Equation 3.26 calculates the VAF the model fitted to the estimate of impulse response function generated through the linear stochastic system identification. The VAF in Figure 3-4 is 96.8%. The state-space impulse response function was also plotted to confirm that the time based impulse response function from the state-space dynamic model description was calculated correctly (i.e., algebra check).

$$\text{VAF} = 100\left(1 - \frac{\sigma\left(h_{\text{model}} - h_{\text{Est}}\right)^2}{\sigma\left(h_{\text{Est}}\right)^2}\right) \tag{3.26}$$

where $\sigma(x)$ is the standard deviation operator, $\sigma(x) = \sqrt{\frac{1}{n}\Sigma_{i=0}^{n-1}\left(x_i - \mu\right)^2}$, μ is the mean, h_{model} is the fitted model impulse response function, and h_{Est} is the estimated impulse response function using linear stochastic system identification techniques.

Finally Table 3.2 compares the calculated model values with the fitted values achieved during the fit performed in Figure 3-4. The fitted values, with the exception of C_1 and C_2, fall within the calculated ranges, and even C_1 and C_2 are near the predicted values. Although Equations 3.21-3.25 define the expressions for C_1 and C_2, in a real system definitions of where C_1 ends and C_2 begins does not necessarily need to match the definitions in Figure 3-1. In addition, a second plausible explanation

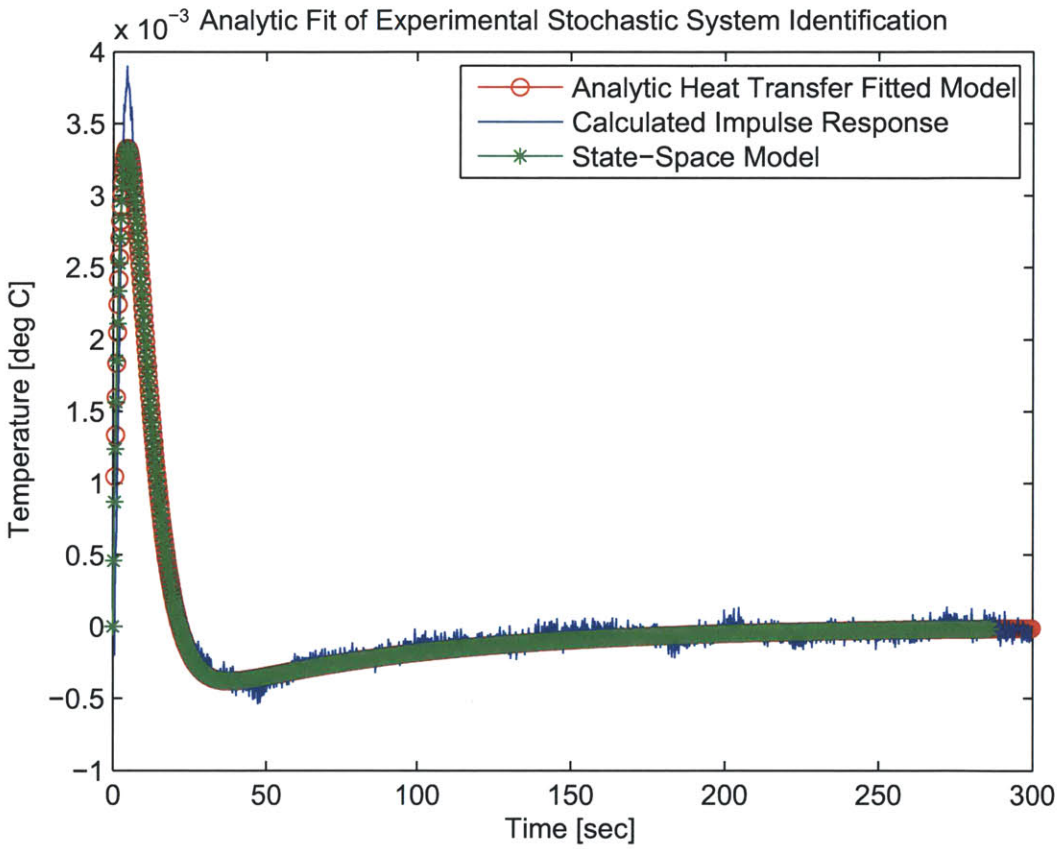

Figure 3-4: Non-parametric, parametric, and state-space impulse response functions for the calorimeter from Ni RTD input to Thermopile output.

Table 3.2: Comparison between non-linear least squares fitted parameters and calculated parameters based on material and geometric properties of the calorimeter.

Parameter	Fit	Calculated	Units
C_1	0.072	0.078-0.110	J/K
C_2	0.340	0.150-0.280	J/K
R_1	81	36-180	K/W
R_2	440	180-460	K/W
R_3	320	180-460	K/W

for the discrepancy of C_1 and C_2 from the fitted values may be due to the reported material properties used in the calculation. Because the calculated values match the fitted values so well, the analytic model can be used with greater confidence going forward to improve the calorimeter design. This model points to two methods of improving the disturbance rejection of the calorimeter: 1) better matching of R_2 and R_3 and 2) improved control of the base temperature T_B. The improvement of temperature control is discussed in the next chapter.

Chapter 4

Temperature Control

To perform sensitive calorimeter measurements, it is important to precisely control temperature. In choosing a temperature sensor for temperature control, three main criteria were considered: 1) high linearity (to facilitate controller design), 2) sensitivity, and 3) availability. From the list in Table 2.2, thermistors and RTDs were investigated as potential feedback sensors for temperature control. While thermistors are more sensitive than RTDs at room temperature, their significant non-linear behavior complicates controller design over a large temperature range (20-80^{0}C). To compensate for the relative lack of sensitivity, an RTD was chosen for the calorimeter temperature feedback sensor. Ni RTDs have a temperature sensitivity that is roughly twice that of the ubiquitous platinum RTD (6720 ppm/^{0}C vs. 3850 ppm/^{0}C). Because nickel easily oxidates at higher temperatures it has a reduced recommended temperature range (-60-250^{0}C vs. -70-650^{0}C). However, for this specific application the sacrificed temperature operating range does not limit the performance of a biochemical calorimeter.

There are two common ways to measure a resistance: 1) bridge circuit topology and 2) current source topology. Both methods were explored in this work and are described in the following sections.

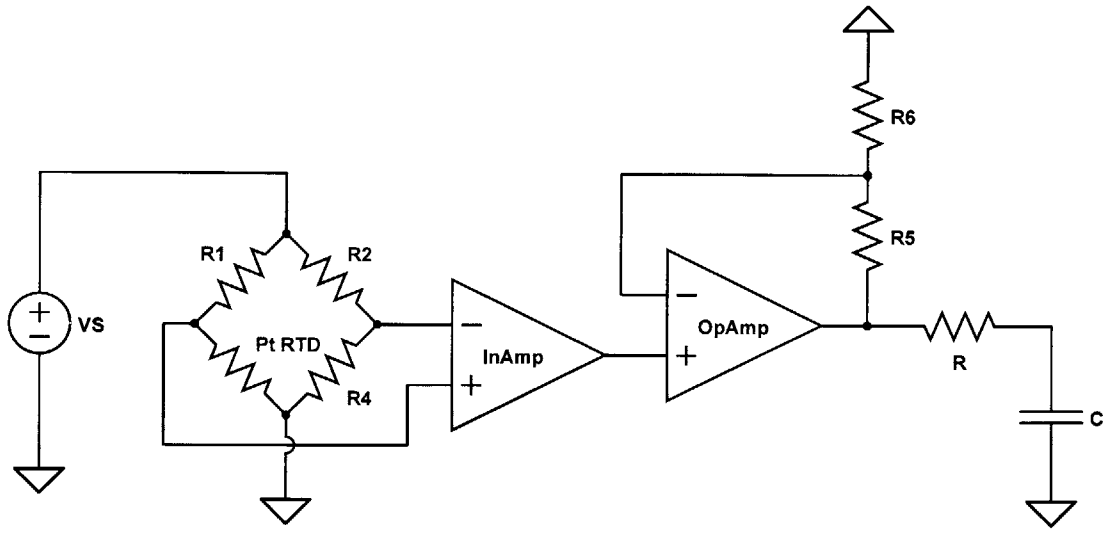

Figure 4-1: Simple RTD bridge circuit diagram.

4.1 Two-Wire Bridge RTD

Figure 4-1 displays an analog circuit to measure the resistance change of RTD due to a temperature change. While this is a simple circuit, a noise analysis was performed to predict the potential sensitivity of the circuit. While a Ni RTD was ultimately chosen, as mentioned above, for the temperature feedback sensor for this study, initially a platinum RTD was used.

To estimate the noise of this circuit, first the noise of the bridge and instrumentation amplifier stage was analyzed. Instrumentation amplifiers have four main noise sources: 1) resistor noise, 2) current noise, 3) input noise, and 4) voltage noise [16]. Equation 4.1 demonstrates how to compute the resistor noise referred to one of the inputs of the instrumentation amplifier, which has units of $V/\sqrt{\text{Hz}}$.

$$v_{\text{N,Res}} = \sqrt{4k_B T R_{\text{Eq}}} \tag{4.1}$$

where $v_{\text{N,Res}}$ is the instrumentation amplifier resistor input noise, k_B is Boltzmann's constant ($k_B = 4.138 \times 10^{-23}$ J/K), T is the absolute temperature in K, and R_{Eq} is the input impedance of the input of the instrumentation amplifier (the input impedance of the positive input is $R_2//R_4$ and $R_1//R_3$ for the negative input).

Hence, Equation 4.2 displays the total resistor noise referred to the instrumentation amplifier input, $v_{\mathrm{T,Res}}$ for the instrumentation amplifier. This assumes the the resistor noise is Gaussian and uncorrelated such that the sum of the resistor noise is not the linear sum but rather the square root of the sum of the squares.

$$v_{\mathrm{T,Res}} = \sqrt{\left(\sqrt{4k_BT(R_1//R_3)}\right)^2 + \left(\sqrt{4k_BT(R_2//R_4)}\right)^2} \tag{4.2}$$

Equation 4.3 calculates the current noise, $v_{\mathrm{N,Cur}}$ for each instrumentation amplifier input.

$$v_{\mathrm{N,Cur}} = R_{\mathrm{Eq}} i_N \tag{4.3}$$

where i_N is the current noise with units of $A/\sqrt{\mathrm{Hz}}$ and typically found in the instrumentation amplifier data sheet.

Similar to the total resistor noise referred to the input, the total current noise, $v_{\mathrm{T,Cur}}$, is calculated in Equation 4.4

$$v_{\mathrm{T,Cur}} = \sqrt{((R_1//R_3)i_N)^2 + ((R_2//R_4)i_N)^2} \tag{4.4}$$

The input voltage noise, $v_{\mathrm{N,Input}}$ is typically listed in the instrumentation amplifier data sheet. Likewise, the output voltage noise, $v_{\mathrm{N,Output}}$, is also listed in the data sheet. To refer the noise to the input, divide by the gain of the amplifier, G. Therefore the total noise in the bridge and instrumentation amplifier referred to the input, $v_{\mathrm{N,Total}}$, is calculated in Equation 4.5.

$$v_{\mathrm{N,Total}} = \sqrt{(v_{\mathrm{T,Res}})^2 + (v_{\mathrm{N,Cur}})^2 + (v_{\mathrm{N,Input}})^2 + \left(\frac{v_{\mathrm{N,Output}}}{G}\right)^2} \tag{4.5}$$

This total noise number is the spectral noise and has units of $V/\sqrt{\mathrm{Hz}}$. A closer examination of Equation 4.5 reveals that all of the terms with the exception of $v_{\mathrm{N,Input}}$ can be reduced through careful circuit design choices (i.e., smaller bridge resistors and a large gain). As a result, a good design will have a total spectral noise that is close to the input spectral noise of the amplifier. The second key piece to a low noise design is

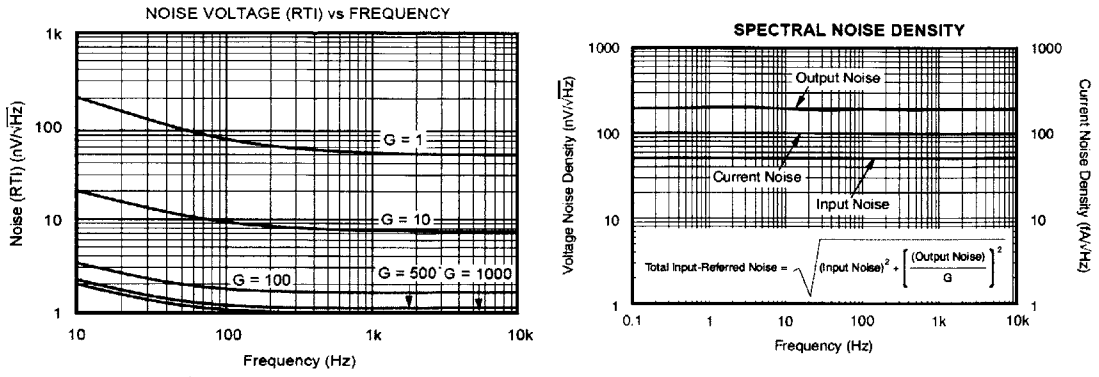

Figure 4-2: Spectral noise plots for two Texas Instrument instrumentation amplifiers, INA 163 on the left and INA333 on the right.

the selection of the instrumentation amplifier. However, it is critical to consider the shape of the spectral noise of the amplifier. Equation 4.6 calculates the root mean squared (RMS) voltage noise, $v_{\text{N,Total-RMS}}$, of the bridge and instrumentation amplifier circuit.

$$v_{\text{N,Total-RMS}} = \sqrt{\int_{f_1}^{f_2} (v_{\text{N,Total}}(f))^2 \, df} \tag{4.6}$$

where f_1 and f_2 are the lower and upper measurement bandwidth frequencies.

Figure 4-2 contains two different spectral density plots for two different Texas Instruments instrumentation amplifiers. Many amplifiers display $1/f$ noise at low frequencies (as shown in the left spectral density plot of Figure 4-2), a noise whose amplitude is inversely proportional to frequency. Because of Equation 4.6, in low bandwidth applications, it is often desirable to choose a an amplifier that does not exhibit any $1/f$ noise, such as that on the right in Figure 4-2. Even though Texas Instruments INA333 has an input voltage spectral noise density of 50 nV/$\sqrt{\text{Hz}}$, that noise integrated from DC to 1 Hz is less than the integrated noise from the INA163 over the same bandwidth, despite a much lower reported input voltage spectral density of 1 nV/$\sqrt{\text{Hz}}$.

Finally if the spectral density is constant in the bandwidth of interest, Equation 4.6 simplifies to Equation 4.7

$$v_{\text{N,Total-RMS}} = \left(K_{\text{Filter}}\sqrt{f_2 - f_1}\right) v_{\text{N,Total}} \tag{4.7}$$

where K_{Filter} is a constant to account for the non-brickwall nature of the circuit's filter. For a single pole filter, $K_{\text{Filter}} = 1.57$.

In addition to the noise analysis performed on the instrumentation amplifier, a similar noise analysis can be performed on the non-inverting operational amplifier stage. However, as long as the output referred noise (i.e., $Gv_{\text{N,Total-RMS}}$) of the instrumentation amplifier stage is 3-5 times greater than the input referred noise of the non-inverting operational amplifier stage, one can ignore the noise contributions of the non-inverting operational amplifier stage. Again this assumes that the noise is Gaussian and uncorrelated such that these two noise sources sum as the square root of the sum of the squares. As a result, if the prior stage's output noise is 3-5 times greater than the input noise of the next stage, the next stage will maximally contribute only an additional 10% to the total noise; therefore, it can be neglected. In this study the non-inverting operational amplifier stage was designed such that the noise of the instrumentation amplifier stage would dominate.

Equation 4.8 calculates the total RMS noise at the A/D input. Similar to the non-inverting operational amplifier stage, the data acquisition system was chosen such that its noise was 3-5 less than the total noise of the RTD circuit.

$$v_{\text{N,RTD-Circuit-RMS}} = G\left(1 + \frac{R_5}{R_6}\right) v_{\text{N,Total-RMS}} \tag{4.8}$$

where $\left(1 + \frac{R_5}{R_6}\right)$ is the gain of the non-inverting operational amplifier stage in Figure 4-1.

Finally, now that the performance of the circuit can be modeled electrically, it is important to connect the electrical noise to the estimated temperature noise. Equation 4.9 is the Callender-Van Dusen equation that relates the temperature of an RTD to the resistance.

$$R_{\text{RTD}} = R_0\left(1 + AT + BT^2\right) \tag{4.9}$$

where R_{RTD} is the resistance of the RTD, R_0 is the nominal resistance of the RTD at a reference temperature (typically 0^0C), and A and B are experimentally determined constants.

Differentiate Equation 4.9, ignore the higher order terms, and substitute into Ohm's law. Then a relationship between voltage noise and temperature noise can be determined (see Equation 4.12).

$$\frac{dR_{\mathrm{RTD}}}{dT} = R_0 A \tag{4.10}$$

$$\Delta R = \frac{v_{\mathrm{N,Total\text{-}RMS}}}{I} \tag{4.11}$$

$$T_N = \frac{\left(\frac{v_{\mathrm{N,Total\text{-}RMS}}}{I}\right)}{R_0 A} \tag{4.12}$$

where I is the current through the RTD ($I = \frac{V_S}{R_1+R_3}$) and T_N is the equivalent temperature noise.

Figure 4-3 displays the results of a 24-hour test of the RTD bridge circuit. A temperature stable 130 Ω resistor (0.5 ppm/^{0}C) was used to simulate an RTD so the noise performance of the circuit could be measured. The standard deviation was calculated for each 1-hour run and varied between 15-25 uV (16 uV calculated - see Table 4.1). The analysis performed above captured the short-term noise amplitude of the circuit remarkably well. However, there is a significant long-term drift exhibited by the circuit, which is even higher when people are present in the building. The 10 runs that demonstrate the least amount of long-term drift occurred between the hours of 10 pm - 6 am. After an exhaustive search for the cause of the long-term drift, the copper leads that connected the circuit to the RTD simulation resistor were identified as the source.

A common technique to minimize the long-term drift that is due to the wire leads is to implement a four-wire resistance measurement topology. The next section will discuss a four-wire current source resistance measurement topology.

Table 4.1: Component and calculated values of RTD bridge circuit. A Texas Instrument INA333 was chosen for the instrumentation amplifier.

Parameter	Value	Units
V_S	2.048	V
R_1	1000	Ω
R_2	100	Ω
R_3	1000	Ω
R_4	100	Ω
R_5	1000	Ω
R_6	1000	Ω
A	0.385	$1/^0$C
i_N	100	fA/$\sqrt{\text{Hz}}$
$v_{\text{N,Input}}$	50	nV/$\sqrt{\text{Hz}}$
$v_{\text{N,Output}}$	200	nV/$\sqrt{\text{Hz}}$
G	100	n/a
K_{Filter}	1.57	n/a
f_1	0 (DC)	Hz
f_2	1	Hz
R_{Eq}	107	Ω
$v_{\text{T,Res}}$	1.8	nV/$\sqrt{\text{Hz}}$
$v_{\text{T,Cur}}$	0.015	nV/$\sqrt{\text{Hz}}$
$v_{\text{N,Total}}$	50.1	nV/$\sqrt{\text{Hz}}$
$v_{\text{N,Total-RMS}}$	79	nV RMS
$v_{\text{N,RTD-Circuit-RMS}}$	16	μV RMS
T_N	120	$\mu^0 C$

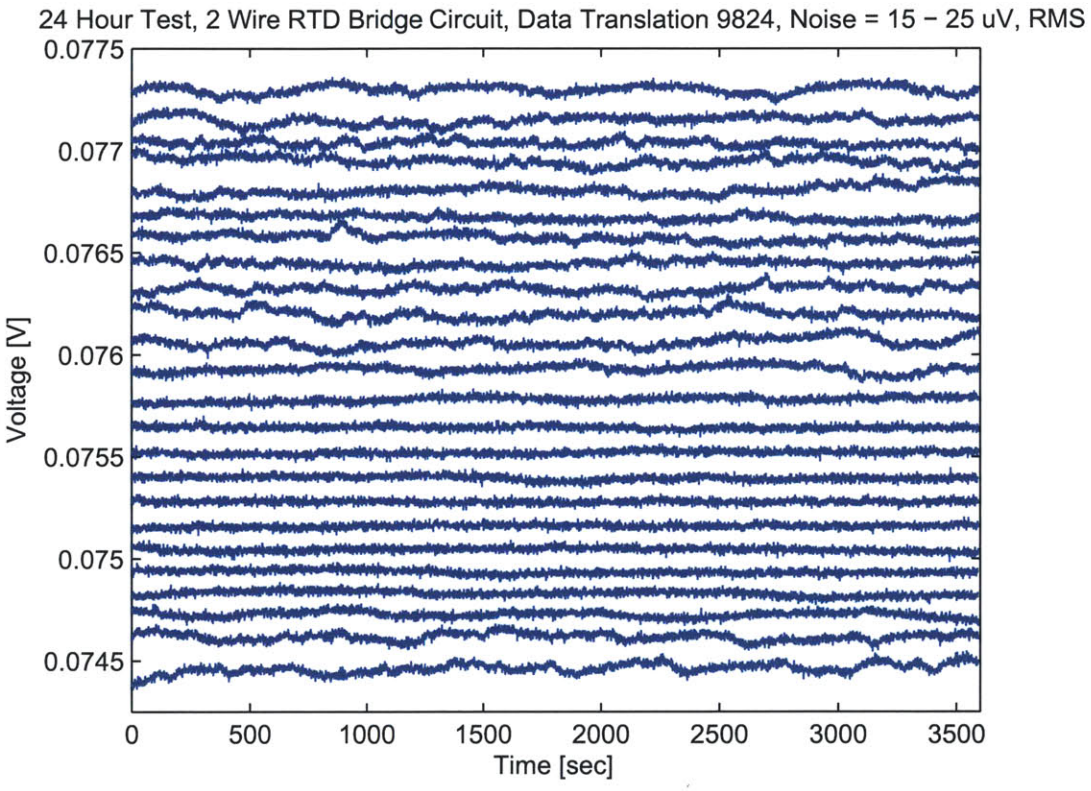

Figure 4-3: A 24-hour test, each 1-hour trace is mathematically offset from the previous trace, of the temperature stability of a two wire RTD bridge measurement circuit.

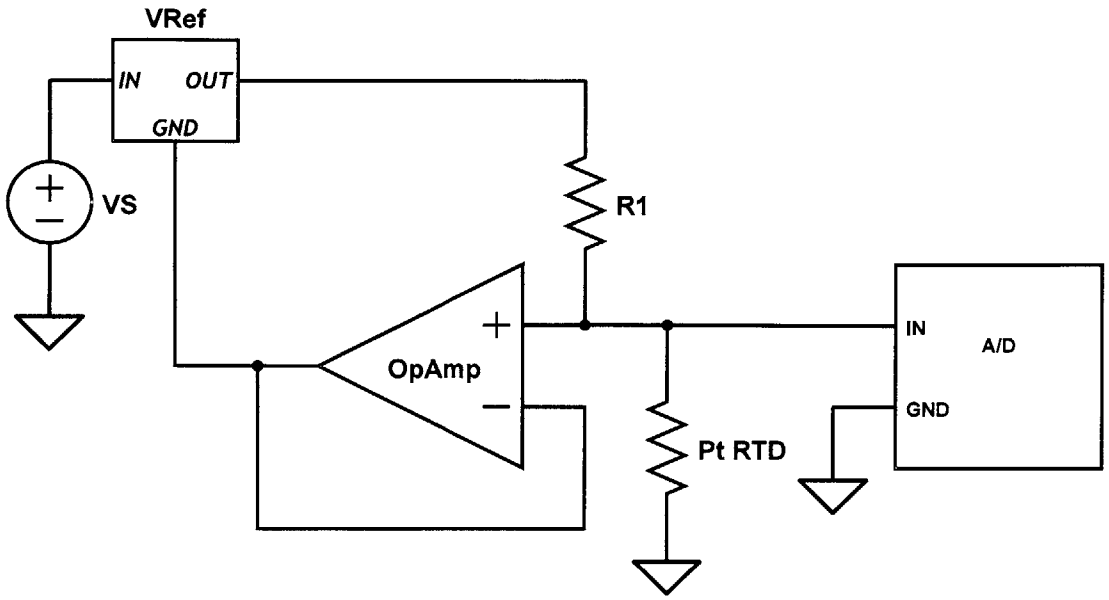

Figure 4-4: Simple schematic of how to perform a four-wire resistance measurement using a low-noise current source (see [28]).

4.2 Four-Wire Current Source RTD

Figure 4-4 displays a simple schematic for a four-wire current source resistance measurement. As long as the input impedance of the voltage measurement is very high, no current will flow through the measurement leads, and regardless of the resistance changes due to temperature of those leads, there is no corresponding voltage drop. As a result, the noise of the circuit is simple to calculate (see Equation 4.13)

$$v_{\mathrm{N,Cur}} = R_{\mathrm{RTD}} i_{\mathrm{N,Cur}} \tag{4.13}$$

where $v_{\mathrm{N,Cur}}$ is the voltage noise of the measurement, R_{RTD} is the resistance of the RTD, and $i_{\mathrm{N,Cur}}$ is the noise of the current source.

However, depending on the current source circuit implemented, it is difficult to estimate the noise of the current source, $\imath_{\mathrm{N,Cur}}$. In addition, there are limitless current source circuit topologies. After a literature search, a current source design was adopted from a Burr-Brown (now part of Texas Instruments) application note [28].

Similar to the previous 24-hour RTD circuit test (see Figure 4-3), Figure 4-5

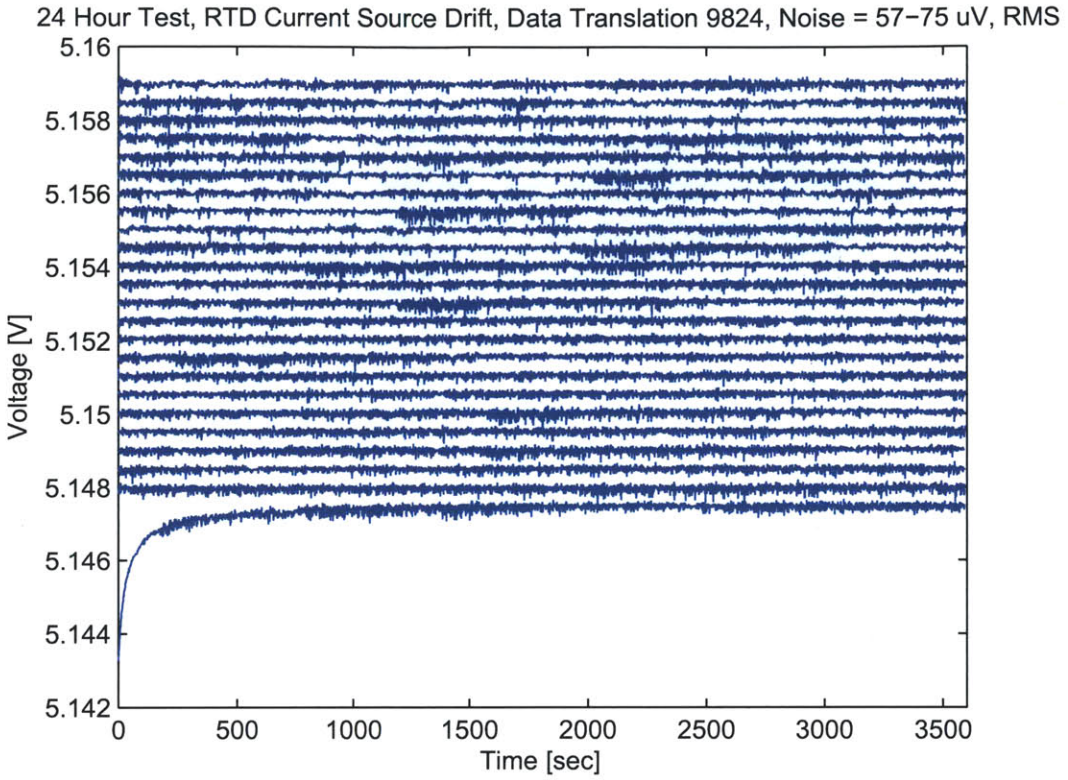

Figure 4-5: A 24-hour test, each 1-hour trace is mathematically offset from the previous trace, of the temperature stability of a current source RTD measurement circuit.

displays the results of a 24-hour circuit test for the four-wire current source RTD measurement circuit. While the circuit does not exhibit any long-term drift as expected from a four-wire measurement, the short-term noise is significantly higher than the previous two-wire bridge measurement.

In the next section, the combination of a bridge circuit with a four-wire measurement will be addressed with the goal of high sensitivity, but low long-term drift.

4.3 Four-Wire Bridge RTD

Finally, to combine the sensitivity advantages of a bridge circuit design and the minimal long-term drift advantages of a four-wire design, a hybrid four-wire bridge topology was designed and tested. While this is not a new topology, it is uncommon.

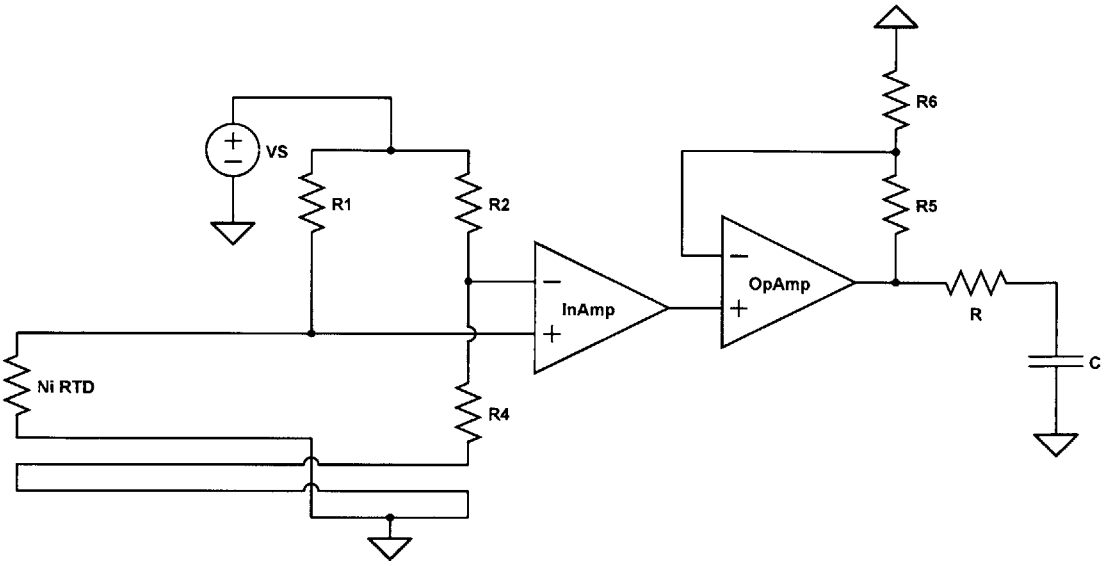

Figure 4-6: Hybrid circuit topology including bridge and four-wire characteristics.

Figure 4-7 contains a diagram of the bridge portion of the new circuit. A bridge circuit amplifies the difference in voltage between the two legs of the bridge, which is due to the resistance differences between the legs. However, common mode changes, those changes that are common to both legs, will not be amplified. As a result, to minimize/eliminate the impact of test lead resistance changes, due to temperature fluctuations, one strategy is to ensure that both legs experience the same changes. Therefore in the construction of this circuit, the leads leading to the RTD were made of a four conductor twisted wire assembly, two to connect to the RTD, and two that were soldered for continuity near the RTD.

In addition, a nickel RTD was implemented in the this hybrid circuit to further increase the temperature sensitivity of the measurement. Since the sensitivity of the a Ni RTD is about twice that of a Pt RTD, the gain of the instrumentation amplifier was reduced from 100 to 50. As a result, the estimated noise of this noise circuit was 8 μV RMS or 72 μ^0C, not 16 μV RMS or 120 μ^0C that was calculated for the two-wire Pt RTD bridge circuit (see Table 4.1). Figure 4-7 displays the results of a 16-hour test, conducted in the same manner as the 24-hour test discussed previously. Not surprisingly the new Ni RTD circuit is roughly two times more sensitive than the

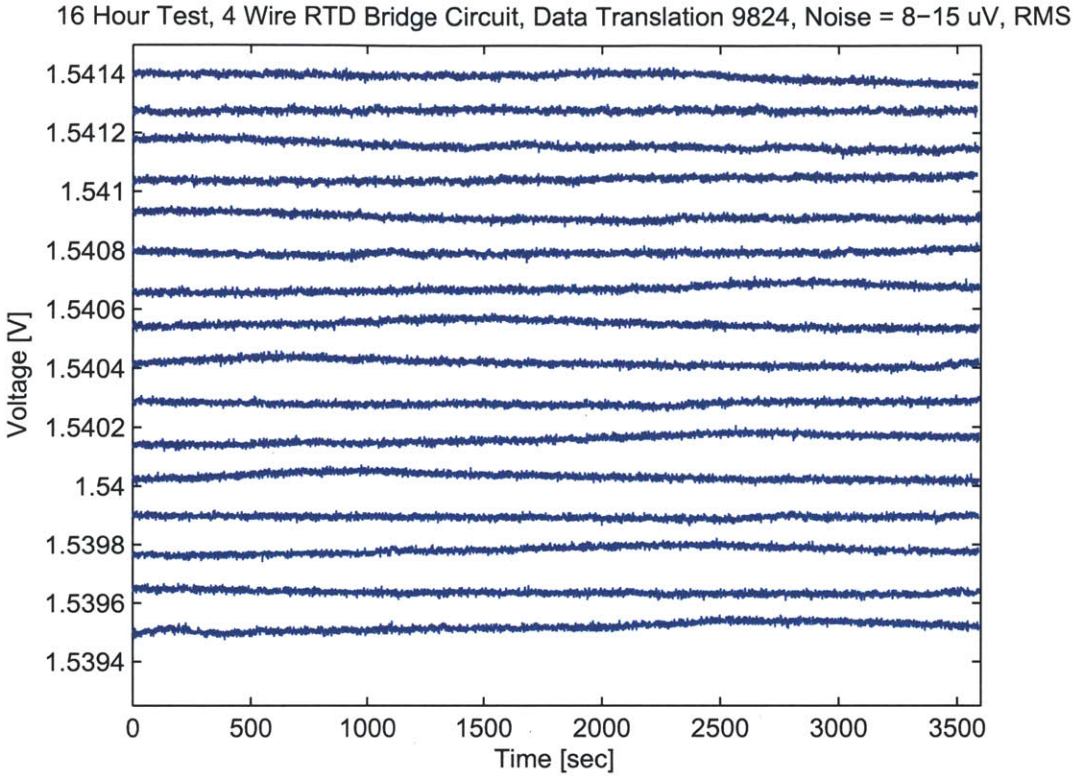

Figure 4-7: A 16-hour test, each 1-hour trace is mathematically offset from the previous trace, of the temperature stability of a four-wire RTD bridge measurement circuit.

previous Pt RTD circuit. The long-term stability has also been significantly reduced. While attempts to ensure that the leads were thermally coupled together as best as possible, clearly it is not perfect since there is still some remaining long-term drift in the circuit.

Table 4.2 summarizes the modeling and measured results for the three designed RTD measurement circuits.

Now that a suitable temperature feedback sensor has been identified, the digital

Table 4.2: Summary of RTD modeled and experimental results.

Circuit Topology	Modeled Value	Measured Value
Two-wire Pt RTD bridge circuit	16 μV	$18 \pm 4.3\mu$V
Four-wire current source Pt RTD circuit	n/a	$64 \pm 5.7\mu$V
Four-wire Ni RTD bridge circuit	8 μV	$11 \pm 2.6\mu$V

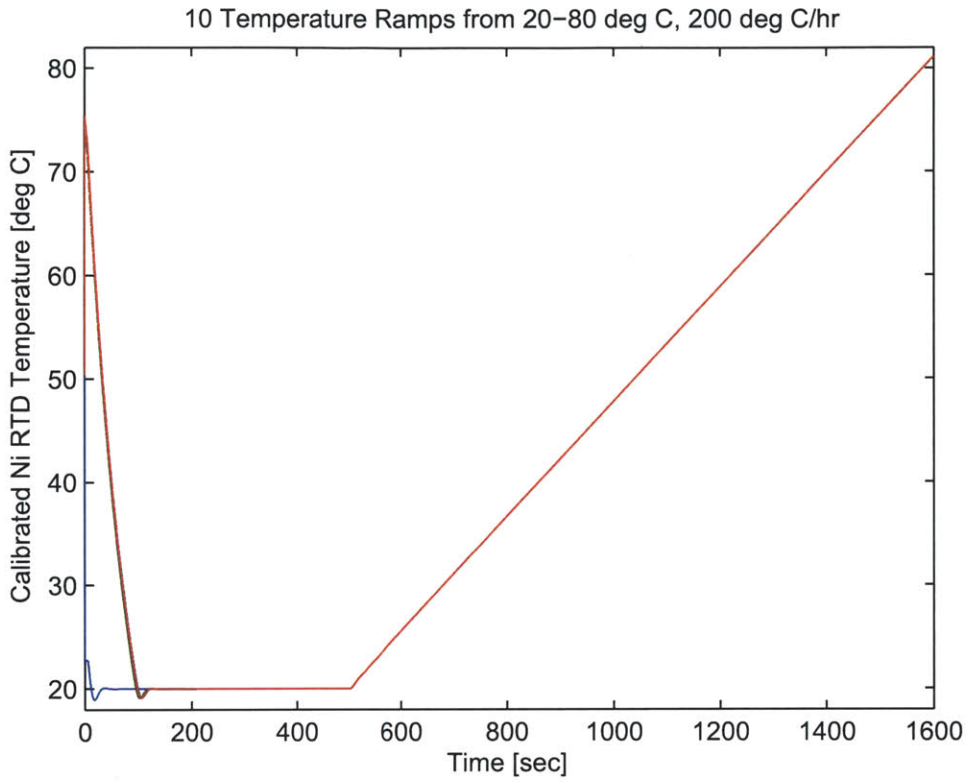

Figure 4-8: Ten calorimeter temperature ramps, 20-80^{0}C, at 200^{0}C/hr

controller that was designed to perform the temperature ramp will be discussed.

4.4 Temperature Controller Design and Performance

A simple digital PID controller was used to control temperature in this calorimeter. The PID controller was tuned using Ziegler-Nichols tuning methods [42]. Figure 4-8 displays 10 temperature ramps from 20-80^{0}C, where were scanned at 200 deg/hr. Before each scan was started the calorimeter thermostated at 20^0 C for 500 seconds. In addition, scans 2-10 (scan 1 is the blue trace) required significantly more time to return to 20^0 C. This is due to the subsequent runs cooling from the previous 80^0 ending temperature from the previous scan.

Figure 4-9 displays the temperature error (command - measured) for Figure 4-8. During the ramping phase of the scan, there is steady-state error. This is not

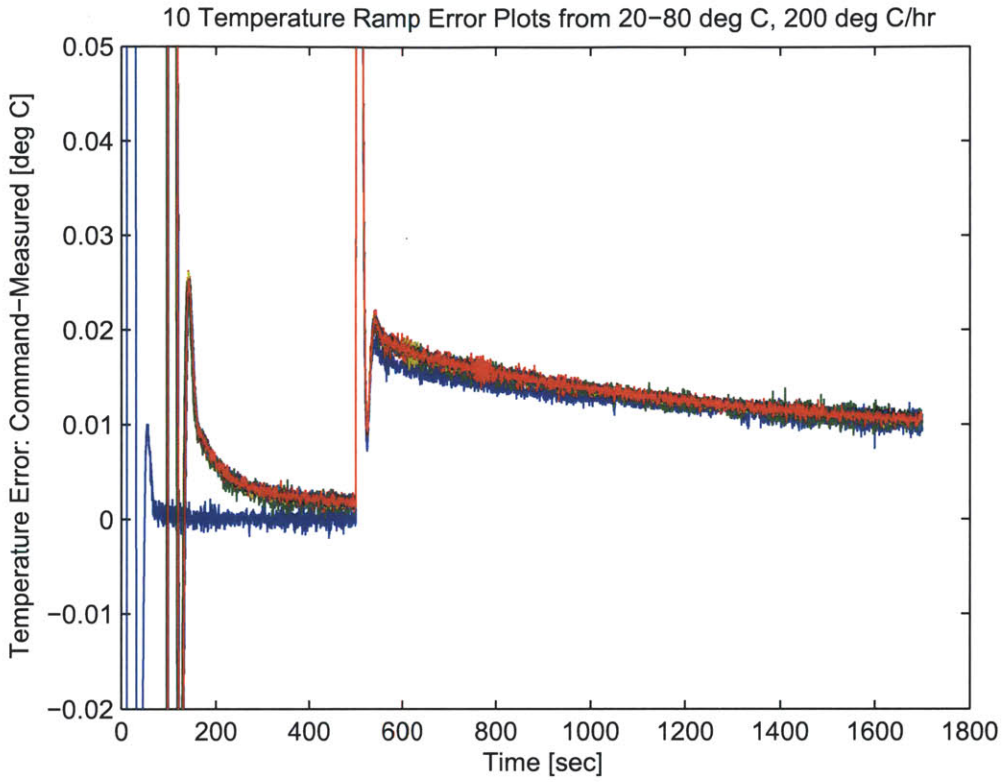

Figure 4-9: Ten calorimeter temperature ramp error plots, 20-80^{0}C, at 200^{0}C/hr. The short-term temperature noise average is 406 μ^0C.

surprising since a PID controller only has one integrator and in order to have zero steady-state error during a ramp (that is controlling a first order system with no zeros) a second integrator is needed. However, the temperature noise is of more interest than the steady-state error in this application. The average short-term temperature noise during the ramp portion of the signal for all 10 runs is 406 μ^0C. This is roughly six times greater than the estimated noise of the temperature sensor.

The next chapter will discuss the calorimetric results achieved in the final integrated calorimeter.

Chapter 5

Results and Future Work

5.1 Results

One of the goals of this thesis was to develop a calorimeter that is capable of measuring a protein unfolding event with 10 μg of protein. As was mentioned in Section 2.2, RNase A was the biochemical system used to verify the performance of the calorimeter. Figure 5-1 displays four separate RNase A runs at 100, 50, 25, and 12.5 mg/ml. A control run was subtracted from each protein run, as discussed in Section 2.1. In addition, a simple FIR filter processed each run. The last dilution, 12.5 mg/ml of RNase A, is near the detection limit of the current device, and represents 125 μg of protein consumed per experiment for the 10 μl cell. As is common with other instruments and academic efforts, the performance of the device is limited more by long-term drift than short-term noise. This is slightly more than 10 times less sensitive than the original goal. However, this is the first known example of a system that has the potential to be disposable, meaning that the cells could realistically be made for less than a dollar per cell.

Figure 5-2 displays a similar RNase A dilution series as Figure 5-1 but with 10 repeats at each concentration. Although the long-term drift of these 40 experiments is large, the data does demonstrate the repeatability of the entire calorimeter system including the semi-automated fluid handling and temperature control. Part of the long-term drift expressed in these results is mathematically induced. As discussed

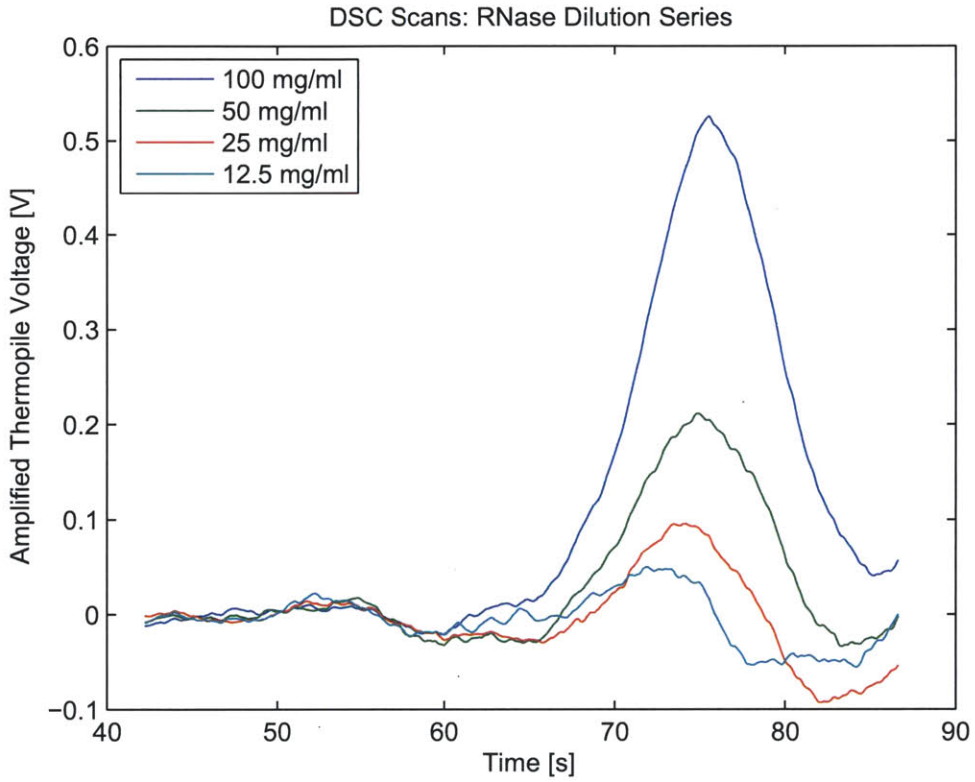

Figure 5-1: Summary of best results achieved on PhD Calorimeter. This plot contains four concentrations of RNase A protein unfolding at 200^0C/hr.

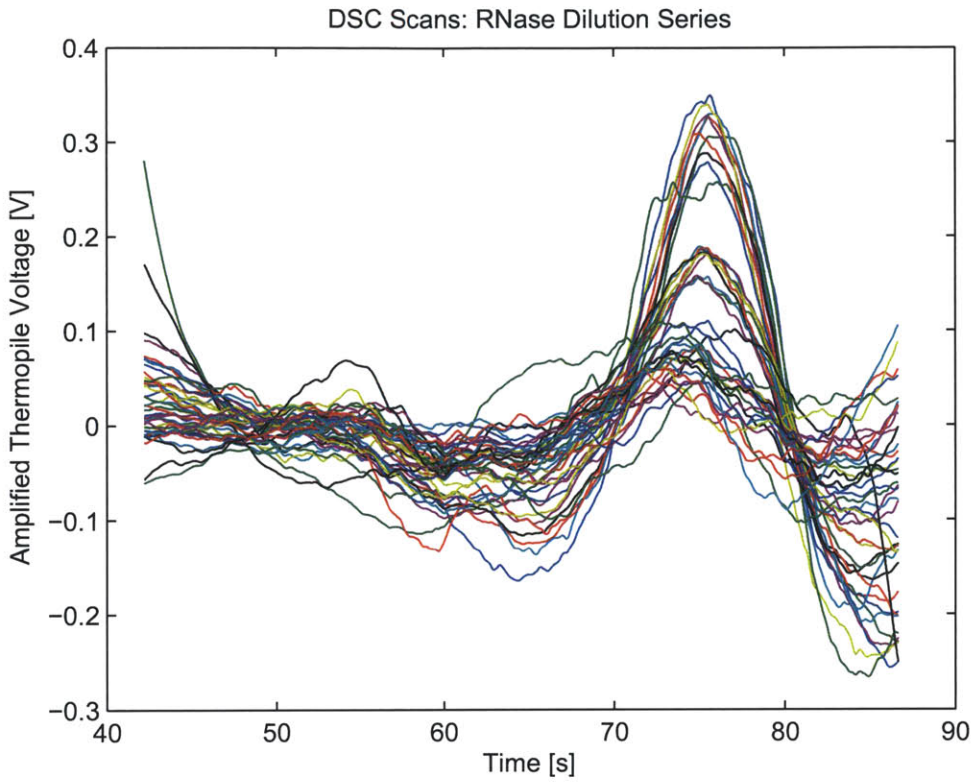

Figure 5-2: 40 repeat RNase A unfolding experiments: 10 at 100 mg/ml, 10 at 50 mg/ml, 10 at 25 mg/ml, and 10 at 12.5 mg/ml.

in Section 2.1, it is common practice to interleave control experiments between each run for subtraction. In these tests, however, no control runs were introduced between each protein run. As a result, a single control run was subtracted from all of the protein runs. While this explains some of the long term drift, it also highlights a long-term performance stability issue of the calorimeter.

5.2 Future Work

In a continuation of this work two main areas need to be addressed:

1. Now that the heat transfer model shows promise in capturing the transient behavior of the calorimeter, it needs to be used to design a better calorimeter.

2. While this study shows that disposable materials can be used in cell construction, additional work must be done to ensure that polymer cells can repeatably be inserted into the calorimeter and generate consistent results.

Chapter 3 showed that an analytic heat transfer model captured more than 96% of the measured impulse response function. In addition, Table 3.2 showed that non-linear least squares fitted values were within or near the ranges predicted by the analytic model. As a result, this model needs to be used with greater confidence to design an improved calorimeter. With a clearer link between design input and calorimeter performance, it may be possible to build a disposable device that consumes less than 10 μg of protein per experiment. In addition to using the model, it will become important to directly measure the material properties of the various calorimeter components.

This study demonstrates the potential feasibility of using polymer materials in calorimeter cell construction; it does not solve all of the remaining technical hurdles required to measure the unfolding behavior of biochemical systems in a repeatable fashion. For example, resistive heaters that are attached to the cell can be replaced by non-contact heating technologies, such as infrared, laser, or inductive heat sources. Also, to increase the reliability and repeatability of thermal interface between the microfluidic cell and the thermopile sensor, a kinematic coupling could be used to bring the two parts into direct contact.

5.3 Summary

In summary, there are two main contributions from this thesis: 1) the feasibility of inexpensive disposable cells has been demonstrated and 2) an analytic heat transfer model has been experimentally verified, which shows how ambient disturbances corrupt the calorimetric measurement. There have been many calorimeters developed that highlight disposability as a design feature. However, the costs of these calorimeters would be too high to be a consumable in an academic or industrial setting. This thesis has shown a method to only make the calorimeter cells disposable, and these

cells could potentially be produced less than one dollar per cell. While there are various analytic models that describe how a calorimeter functions, this is the first known study that models what prevents a scanning calorimeter from achieving the theoretical minimum sensitivity for a thermopile. This model can now be used to better understand what design elements can be changed to further improve the sensitivity of scanning calorimeters.

Appendix A

Calorimeter Source Code

Listing A.1: Calorimeter control script

```
%% Calorimeter Control File
% Scott McEuen, 2013-04-08

close all;
clear all;
clc;

% input parameters
ThermostatTime = 500; % amount of time to wait before ramp
    starts [sec]

%% load feedfoward control parameters into setup
% load('D:\MATLAB\PhD\JacketVolt.mat');
load('D:\MATLAB\PhD\JacketVolt2.mat');
TimeTable = PartTime; % comment out if using JacketVolt.mat

%% Setup experiment
Fs1 = 5350;
% Fs1 = 5;
Fs2 = 5;
FIRLength = 1070;
% FIRLength = 1;
StopTime = 1100+ThermostatTime;
% StopTime = 500+ThermostatTime;
NumExp = 20;

%% turn off DSC event through resistor
% DSConoff = 1;
```

```
% big for loop to run multiple experiments

% preallocation memory
ShortAll = zeros(StopTime*Fs2,NumExp);
DPAll = zeros(StopTime*Fs2,NumExp);
JRTDAll = zeros(StopTime*Fs2,NumExp);
SRTDAll = zeros(StopTime*Fs2,NumExp);
JVoltAll = zeros(StopTime*Fs2,NumExp);
SVoltAll = zeros(StopTime*Fs2,NumExp);
RedTwistVoltAll = zeros(StopTime*Fs2,NumExp);
GreenTwistVoltAll = zeros(StopTime*Fs2,NumExp);
TimeAll = zeros(StopTime*Fs2,NumExp);

for i = 1:NumExp

    % interleave 'buffer' scan with 'protein' scan
    if mod(i,2) == 0

        DSConoff = 1;
%           DSConoff = 0;

    else

        DSConoff = 0;

    end

    % open target simulink models
    open Simulink_PhDControl_v5;
```

```
% compile and load target application on Speedgoat
rtwbuild('Simulink_PhDControl_v5');

% start model and target application that sends workspace
    variables to Speedgoat
tg.start;

pause(StopTime+5);

%% data unpacking from target machine

% Attach to the target PC file system.
f=xpctarget.fs;

% Open the file, read the data, close the file.
h=fopen(f,'data.dat');
TargetData=fread(f,h);
fclose(f,h);

% Unpack the data.
HostData=readxpcfile(TargetData);

Short = HostData.data(:,1);
DP = HostData.data(:,2);
JRTD = HostData.data(:,3);
SRTD = HostData.data(:,4);
JVolt = HostData.data(:,5);
SVolt = HostData.data(:,6);
RedTwistVolt = HostData.data(:,7);
GreenTwistVolt = HostData.data(:,8);
```

```
SetTemp = HostData.data(:,9);
Time = HostData.data(:,10);

%% save data

Location = '\\Microcal2\r&d\Scott\PhD\Data\';
SaveData = [Short DP JRTD SRTD JVolt SVolt RedTwistVolt
    GreenTwistVolt SetTemp Time];

% create indetifying time stamp
Date = clock;
DateStr = [num2str(Date(1)) '-' num2str(Date(2)) '-'
    num2str(Date(3))];
Filename = [DateStr '_' num2str(Date(4)) '-' num2str(Date
    (5)) '_PhDDSC'];

% save data, be careful this will overwrite the same
    filename
% data = [tg.TimeLog tg.OutputLog];
save([Location Filename '.mat'],'SaveData','-mat');

% save all data into large matrix
ShortAll(:,i) = HostData.data(:,1);
DPAll(:,i) = HostData.data(:,2);
JRTDAll(:,i) = HostData.data(:,3);
SRTDAll(:,i) = HostData.data(:,4);
JVoltAll(:,i) = HostData.data(:,5);
SVoltAll(:,i) = HostData.data(:,6);
RedTwistVoltAll(:,i) = HostData.data(:,7);
GreenTwistVoltAll(:,i) = HostData.data(:,8);
```

```
    SetTempAll(:,i) = HostData.data(:,9);
    TimeAll(:,i) = HostData.data(:,10);

end

%% land of plots

figure;
plot(ShortAll(2:end,:));
title('Short');

figure;
plot(DPAll(2:end,:));
title('DP');

figure;
plot(JRTDAll(2:end,:));
title('JRTD');

figure;
plot(SRTDAll(2:end,:));
title('SRTD');

figure;
plot(JVoltAll(2:end,:));
title('JVolt');

figure;
plot(SVoltAll(2:end,:));
title('SVolt');
```

```
figure;
plot(RedTwistVoltAll(2:end,:));
title('RedTwistVolt');

figure;
plot(GreenTwistVoltAll(2:end,:));
title('GreenTwistVolt');

figure;
plot(SetTempAll(2:end,:)-JRTDAll(2:end,:));
title('SetTemp');

figure;
plot(TimeAll(2:end,:));
title('Time');
```

Figures A-1, A-2, and A-3 show pictures of the Simulink model that controlled my PhD calorimeter using a real-time computer.

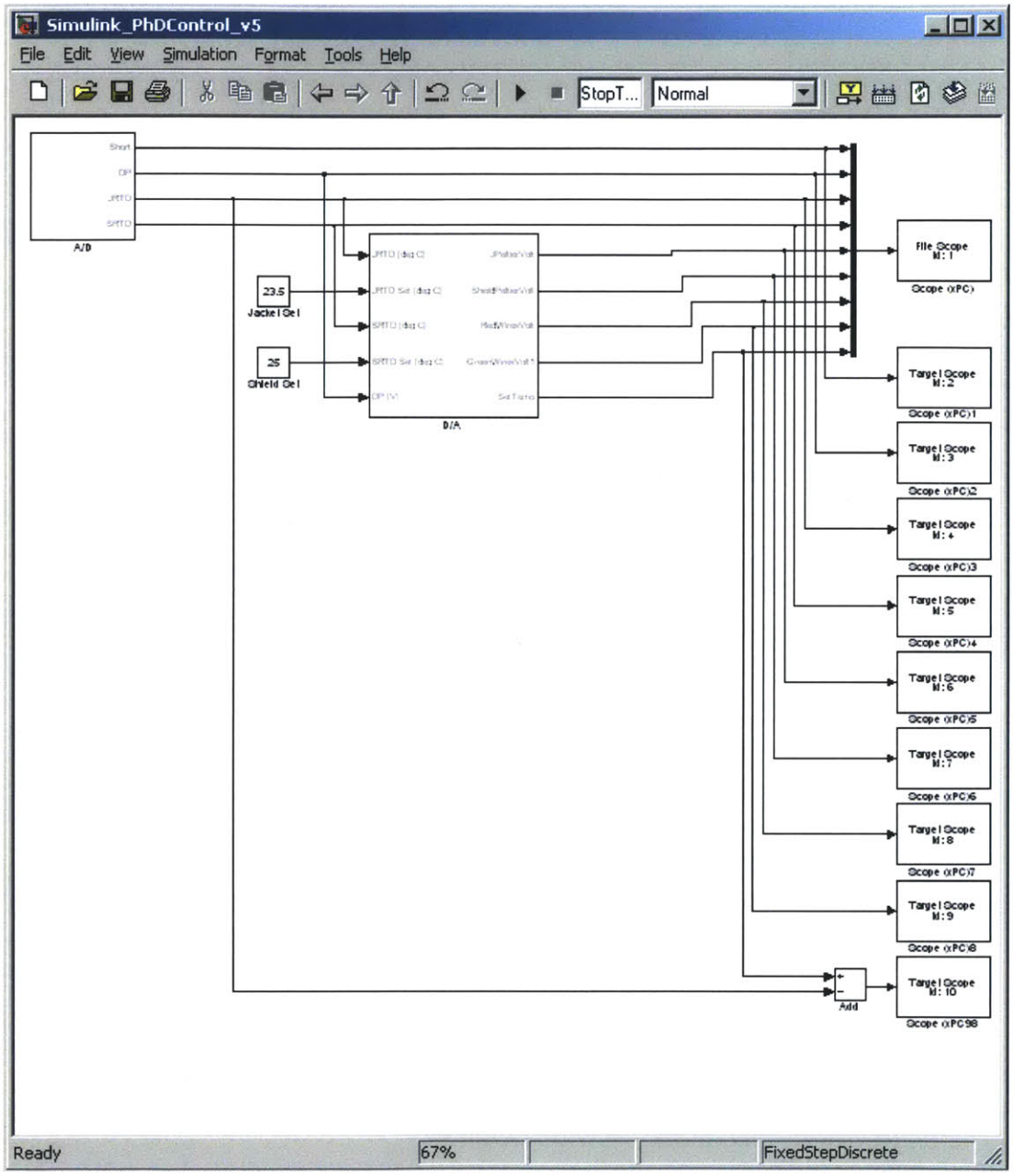

Figure A-1: Simulink model that controlled calorimeter through real-time target computer.

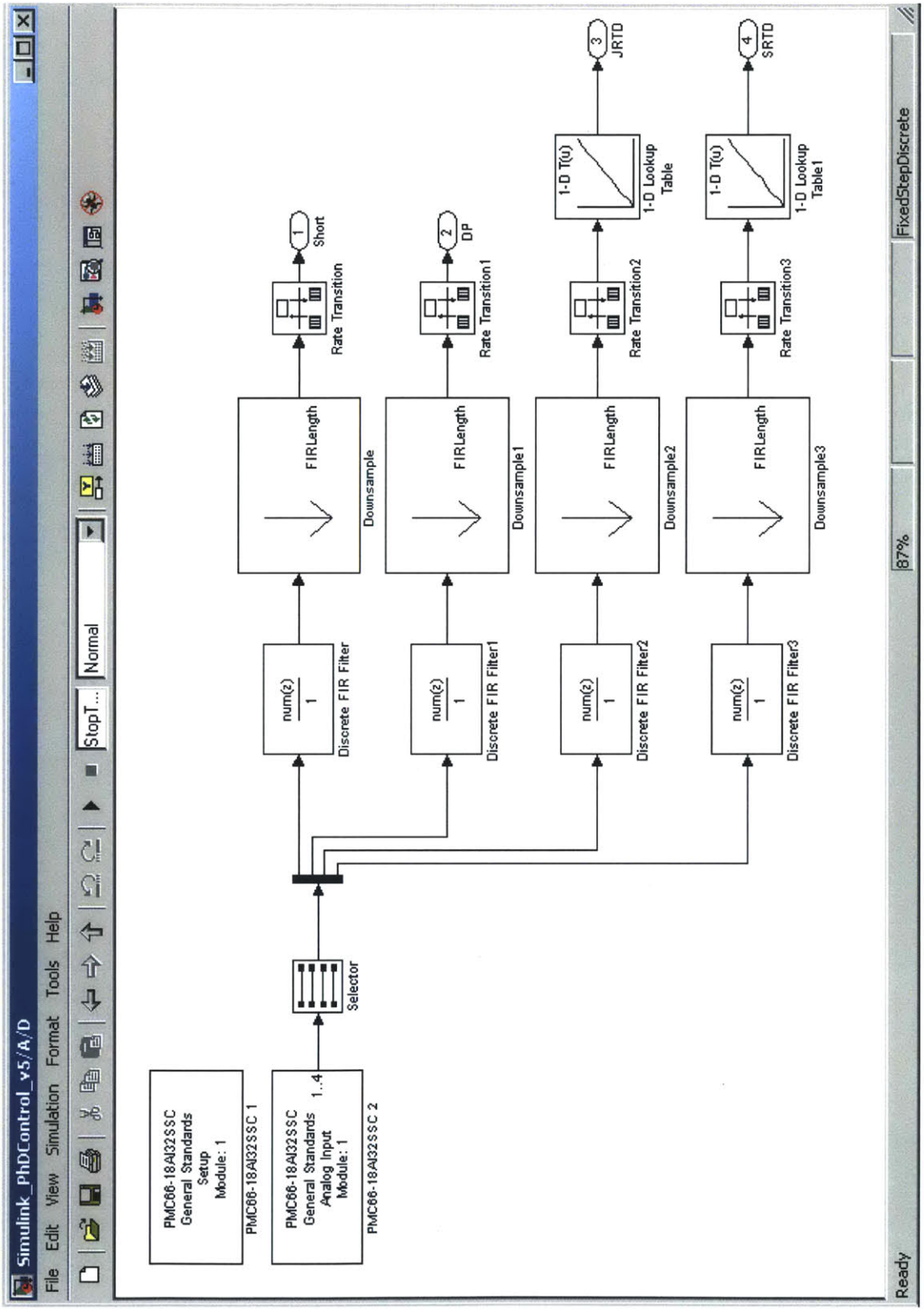

Figure A-2: Simulink model, A/D block, that controlled calorimeter through real-time target computer.

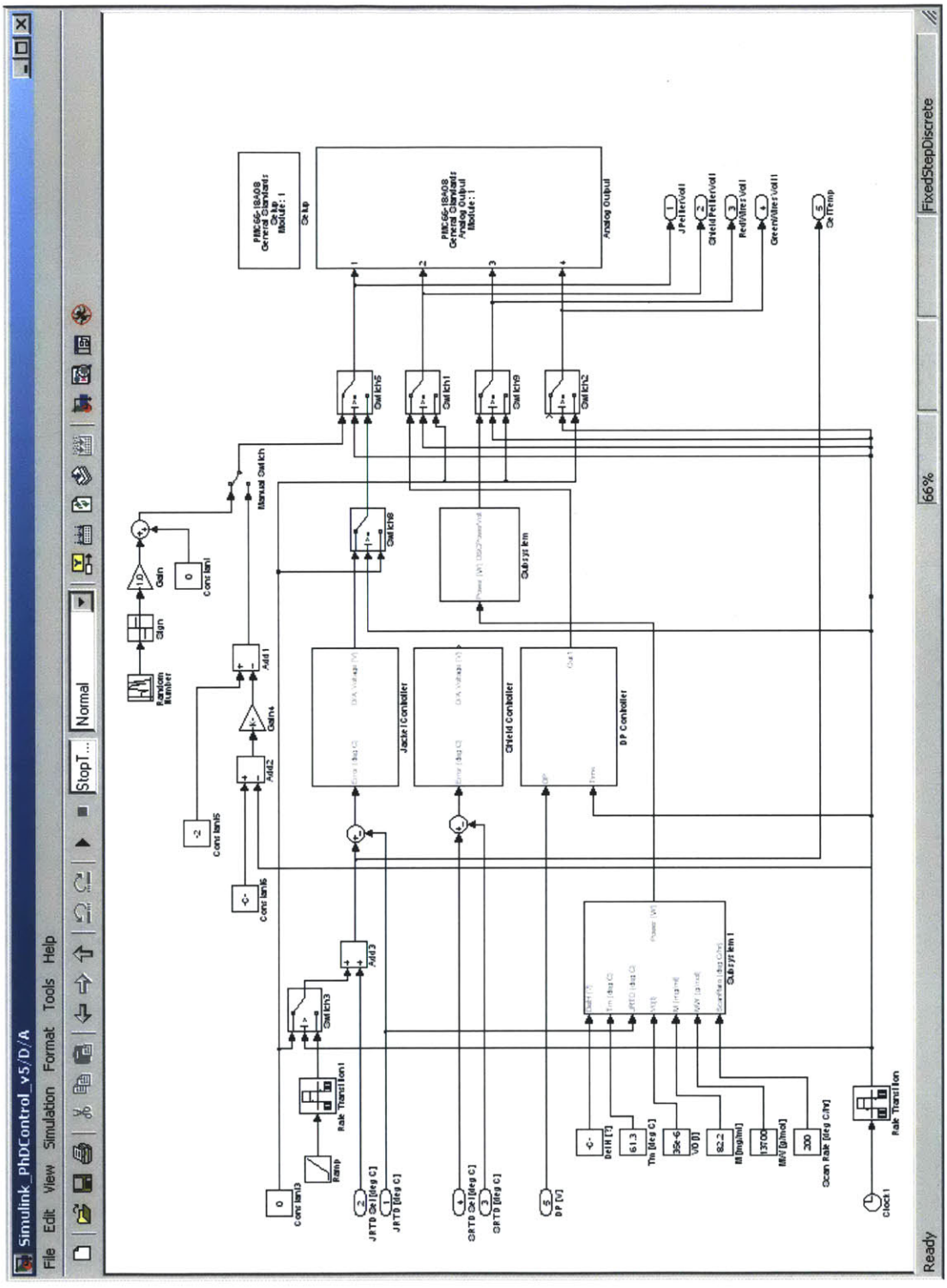

Figure A-3: Simulink model, D/A block, that controlled calorimeter through real-time target computer.

Appendix B

Thermal Model Source Code

Listing B.1: Thermal model: non-linear least squares fitting

```
%% Symbolic Heat Transfer Model
% Scott McEuen, 2013-03-05

close all;
clear all;
clc;

%% Experimental System

%% PhD, Next Generation Analysis
% Scott McEuen, 2012-10-24

close all;
clear all;
clc;

% initialize variables
Fs = 5; % sampling frequency [Hz]
CorLen = 4096;
n = 64;
A10Gain = 10000;
SB = 200e-6;

%% Calculate impulse response

% load('\\Microcal2\r&d\Scott\PhD\Data\2012-12-28_14-57
    _PhDDSC.mat');
load('D:\MATLAB\PhD\Data\2012-12-28_14-57_PhDDSC.mat');
```

```
% load('\\Microcal2\r&d\Scott\PhD\Data\2013-1-30_21-50_PhDDSC
    .mat');

Truncate = 2500;
Input = SaveData(Truncate:end-Truncate,5);
Output = SaveData(Truncate:end-Truncate,2)/(n*SB*A10Gain);
Output = -1*(Output - mean(Output));
Output2 = SaveData(Truncate:end-Truncate,3);
Output2 = -1*(Output2 - mean(Output2));
Time = SaveData(Truncate:end-Truncate,8);
% Time = SaveData(Truncate:end-Truncate,10);
Time = Time-Time(1);

% Calculate impusle response using system ID
[ImpulseTime,Impulse,Freq,Mag,Phase] = SysIDFunction(Time,
    Input,Output,CorLen);

[ImpulseTime2,Impulse2,Freq2,Mag2,Phase2] = SysIDFunction(
    Time,Output2,Output,CorLen);

FunImpulse = Impulse2(4:1500);
FunTime = ImpulseTime2(4:1500);

%% Fit system to experimental data

% condition data to remove first data point (i.e., one second
    time delay)
ImpulseTime = ImpulseTime(1:end-1);
Impulse = Impulse(2:end);
```

```
S = fitoptions('Method','NonlinearLeastSquares','MaxIter',1e6
    ,'TolFun',1e-12,'TolX',1e-12);

% fit Voltage input to DP output (back-calculated to be
    temperature not voltage)
fDP = fittype('a*(-b*exp(-b*x)/((b-c)*(b-d))+c*exp(-c*x)/((b-
    c)*(c-d))+d*exp(-d*x)/((b-d)*(d-c)))','options',S); % note
     that x must be used as the independent variable
[cDP,gofDP] = fit(ImpulseTime,Impulse,fDP,'StartPoint'
    ,[1/10000 1/50 1/500 1/2000])
DPFit = feval(cDP,ImpulseTime);

% fit RTD input to DP output (back-calculated to be
    temperature not voltage)
fFun = fittype('a*(-b*exp(-b*x)/((b-c)*(b-d))+c*exp(-c*x)/((b
    -c)*(c-d))+d*exp(-d*x)/((b-d)*(d-c)))','options',S); %
    note that x must be used as the independent variable
[cFun,gofFun] = fit(FunTime,FunImpulse,fFun,'StartPoint'
    ,[0.25 0.05 0.001 0.5])
FunFit = feval(cFun,FunTime);

% f = fittype('HeatTransferFit(x,C1,C2,R2,R3)','options',S);
f = fittype('HeatTransferFit(x,C1,C2,R1,R2,R3)','options',S);
% f = fittype('HeatTransferFit(x,C2,R1,R2,R3)','options',S);
% [c,gof] = fit(FunTime,FunImpulse,f,'StartPoint',[100e-3 90e
    -3 800 100])
[c,gof] = fit(FunTime,FunImpulse,f,'StartPoint',[100e-3 90e-3
     800 500 500],'Lower',[1e-3 1e-3 10 10 10],'Upper',[1 1
    2500 2500 2500])
```

```
% [c,gof] = fit(FunTime,FunImpulse,f,'StartPoint',[50e-3 1000
    200 150])
DidItWork = feval(c,FunTime);

% calculate the variance accounted for in the model
DPVAF = VAF(Impulse,DPFit)

%% Create Plant Model (based on fit above)

s = tf('s');

% continuous domian model
Plant = cDP.a*s/((s+cDP.b)*(s+cDP.c)*(s+cDP.d));
PlantFun = cFun.a*s/((s+cFun.b)*(s+cFun.c)*(s+cFun.d));

%% Numeric System Number 2

Cap1 = c.C1;
Cap2 = c.C2;
Res1 = c.R1;
Res2 = c.R2;
Res3 = c.R3;

A = [-1/Cap1*(1/Res1+1/Res2) 0 1/(Res2*Cap1);
     0 -1/Cap1*(1/Res1+1/Res3) 1/(Res3*Cap1);
     1/(Res2*Cap2) 1/(Res3*Cap2) -1/Cap2*(1/Res2+1/Res3)];
B = [1/(Res1*Cap1);
     1/(Res1*Cap1);
     0];
C = [1 -1 0];
```

```
D = [0];

Sys = ss(A,B,C,D);

[y,t] = impulse(Sys);

%% Variables

% calculate C1, cells + water
RhoWater = 1000;
RhoCell = 1150; % from DSM Somos 12120 data sheet, www.
    dsmsomos.com
VolWater = 10e-9;
VolCell = 6e-3*5e-3*1.2e-3-VolWater;
CpWater = 4180; % J/kg-K
CpCell = 2100; % 1200-2100 J/kg-K, 10% glass filled
    polycarbonate at www.matweb.com
C1Cal = RhoWater*VolWater*CpWater+RhoCell*VolCell*CpCell;

% calculate C2, sensor
RhoBiTe = 7700; % google search
RhoAlO = 3950; % google search
VolBiTe = 65*2*1.3e-3*500e-6^2;
VolAlO = 2*5e-3*6e-3*500e-6;
CpBiTe = 154; % 154-544 http://www.customthermoelectric.com/
    MaterialProperties.htm
CpAlO = 837; % 837 - 880, matweb http://www.
    customthermoelectric.com/MaterialProperties.htm
C2Cal = RhoBiTe*VolBiTe*CpBiTe+RhoAlO*VolAlO*CpAlO;
```

```
% calculate R1
LStem = 4e-3;
AStem = 1.2e-3^2;
kCell = 0.6; %0.1-0.6 W/m-K www.matweb.com for 10% glass
    filled polycarbonate
hCell = 5; %5-25 W/m^2-K convective heat transfer coefficient
    , natural convection
SACell = (2*pi*10e-3^2+pi*20e-3*25.4e-3)/2; % surface area
    for heat transfer coefficeint half of surface area for one
     side
% ACell = 5e-3*6e-3; % surface area for heat transfer
    coefficeint half of surface area for one side
R1CalCond = LStem/(kCell*AStem)/2;
R1CalConv = 1/(hCell*SACell);

% calculate R2, R3 - assume that kCell is ~ kWater -
    basically true
RSensor = 100;
kTape = 0.60; % 3M 8805 thermally conductive tape
LTape = 125e-6; % thickness
ATape = 5e-3*6e-3; % tape area
LCell = 0.6e-3; % 0.6-1.2e-3 m
ACell = ATape;
R2Cal = RSensor/2+LTape/(kTape*ATape)+LCell/(kCell*ACell);

%% Land of plots

figure;
plot(Time,Input);
title('Hardlimited Stochastic Input');
```

```
xlabel('Time [sec]');
ylabel('Peltier Voltage [V]');

figure;
plot(Time,Output);
title('Temperature Gradient Across Thermopile');
xlabel('Time [sec]');
ylabel('Temperature [deg C]');

figure;
plot(Time,Output2);
title('Absolute Temperature of Silver Base');
xlabel('Time [sec]');
ylabel('Temperature [deg C]');

figure;
plot(ImpulseTime,Impulse);
title('Impulse Response');

figure;
plot(ImpulseTime2,Impulse2);
title('Impulse Response 2');

figure;
plot(ImpulseTime,Impulse,ImpulseTime,DPFit);
xlabel('Time [sec]');
ylabel('Temperature [deg C]');
title('Linear Stochastic SysID: Fitted Impulse Response, VAF
  = 98.9%');
```

```
legend('Experimental','Fitted: zero at origin, three real
    poles','Location','NorthEast');

figure;
plot(FunTime,FunImpulse,FunTime,FunFit);
title('Fun');

FunVAF = VAF(FunImpulse,DidItWork)

figure;
plot(FunTime,DidItWork,'-or',FunTime,FunImpulse,'b',t,y,'-g*'
    )
title('Analytic Fit of Experimental Stochastic System
    Identification');
xlabel('Time [sec]');
ylabel('Temperature [deg C]');
legend('Analytic Heat Transfer Fitted Model','Calculated
    Impulse Response','State-Space Model');
```

Listing B.2: Fitting function called from main thermal model script

```
function [y] = HeatTransferFit(x,C1,C2,R1,R2,R3)
% finds solutions to cubic polynomial for heat transfer
    fitting model

a3 = 1;
a2 = (1/(C2*R3)+1/(C2*R2)+1/(C1*R3)+1/(C1*R2)+2/(C1*R1));
a1 = (2/(C1*C2*R2*R3)+1/(C1^2*R2*R3)+2/(C1*C2*R1*R3)+2/(C1*C2
    *R1*R2)+1/(C1^2*R1*R3)+1/(C1^2*R1*R2)+1/(C1^2*R1^2));
a0 = (2/(C1^2*C2*R1*R2*R3)+1/(C1^2*C2*R1^2*R3)+1/(C1^2*C2*R1
    ^2*R2));
```

```
Q = sqrt((2*a2^3-9*a3*a2*a1+27*a3^2*a0)^2-4*(a2^2-3*a3*a1)^3)
    ;
C = (0.5*(Q+2*a2^3-9*a3*a2*a1+27*a3^2*a0))^(1/3);

% calculate real roots of cubic equation
r1 = -a2/(3*a3)-C/(3*a3)-(a2^2-3*a3*a1)/(3*a3*C);
r2 = -a2/(3*a3)+C*(1+i*sqrt(3))/(6*a3)+(1-i*sqrt(3))*(a2^2-3*
    a3*a1)/(6*a3*C);
r3 = -a2/(3*a3)+C*(1-i*sqrt(3))/(6*a3)+(1+i*sqrt(3))*(a2^2-3*
    a3*a1)/(6*a3*C);

r1 = real(r1);
r2 = real(r2);
r3 = real(r3);

a = (1/(C1^2*R1*R3)-1/(C1^2*R1*R2));
b = -r1;
c = -r2;
d = -r3;

% fitted impluse response function
y = a*(-b*exp(-b*x)/((b-c)*(b-d))+c*exp(-c*x)/((b-c)*(c-d))+d
    *exp(-d*x)/((b-d)*(d-c)));
end
```

Listing B.3: Calculation of impulse response using linear system ID techniques

```
function [ImpulseTime, Impulse, Freq, Mag, Phase] = SysIDFunction
    (Time, Input, Output, CorLen)
% Purpose of Function:
```

```
% 1. Experimentally determine the impulse reponse of
   component, system,
% etc.
% Author: Scott McEuen
% Date: 2011-08-27, converted to function on 2012-03-19
% Technical Reference: Prof. Hunter's Electro-Mechanical
   System: Stochastic
% Binary Input 2.131 notes

% comments
```

```
% 1. NO MORE - Use Agilent 34972A
% 2. NO MORE - Channel 102 is deditcated as analog input
   (34972A) for system ID
% 3. NO MORE - Channel 305 is dedicated as analog output
   (34972A) for system ID
% 4. This will now be done with the new Speedgoat hardware

% inputs
```

```
% 1. Time [sec] - time vector from Simulink
% 2. Input [V] - hard-limited random signal from Simulink
% 3. Output [n/a] - measured output from Simulink
% 4. CorLen [n/a] - number of points in non-parameterized
   impulse

% outputs
```

```
% 1. ImpulseTime [sec] - time vector for impulse response
% 2. Impulse [n/a] - impusle response vector
% 3. Freq [Hz] - frequency domain frequency vector
% 4. Mag [n/a] - magnitude response
% 5. Phase [deg] - phase reponse

%% preliminary data preparation

Fs = 1/mean(diff(Time));
% Fs = 1;
% Output = Output - mean(Output);

%% System ID: Time Domain (2.131 notes)
```

```
% perform correlations
[cxx,lagsxx] = xcorr(Input);
cxx = cxx(find(lagsxx==0):find(lagsxx==0)+CorLen-1);
[cxy,lagsxy] = xcorr(Output,Input);
cxy = cxy(find(lagsxy==0):find(lagsxy==0)+CorLen-1);

% form Toeplitz matrix
Cxx = toeplitz(cxx);

% estimate impulse response
% Impulse = 1/Fs*(Cxx\cxy(1:length(cxx)));
Impulse = Fs.*(Cxx\cxy(1:length(cxx))); % this is the correct
    formula! Fs.* not 1/Fs.*
ImpulseTime = (0:1/Fs:length(Impulse)/Fs-1/Fs)';
```

```
%% System ID: Frequency Domain (MATLAB's tfestimate)
-------------------------------------------------

% [H, FreqRad] = tfestimate(Input, Output, [], [], [], Fs);
[H, FreqRad] = tfestimate(Input, Output);
Freq = FreqRad*Fs/(2*pi);
% Freq = FreqRad/(2*pi);
Mag = abs(H);
Phase = 180/pi*unwrap(angle(H));
end
```

Appendix C

Hardware Iterations

During the development work of this thesis, four main prototype systems were built (see Figures C-1-C-4). In addition, two iterations were made on the first prototype, Figure C-1, and the third prototype, Figure C-3. The data presented in this thesis was produced entirely by the second iteration of the third prototype. A brief description of each prototype will be provided below.

Virtually all of the thermopile based calorimeters listed in Table 1.1 are setup in a twinned or matched reference and sample cell design. However, other than qualitative symmetry arguments the literature does not model or predict the performance of such a design. As a result, the main goal of the first prototype, Figure C-1, was to understand the performance ramifications of a single cell design. A single cell design is significantly easier to manufacture than a twinned cell design. Furthermore, the cell was made from three separate 316 stainless pieces. The pieces were cut on a micro water-jet and then joined with adhesive. The cell was designed such that conductive heat transfer would dominate. However, the performance of this prototype was not sufficient to proceed further.

The main goal of the second prototype, Figure C-2 was to minimize the influence of ambient temperature disturbances on the calorimetric measurement. In the picture there are two main center square features that hold two separate thermopile senors between the sample and reference cell. The idea was to use the middle square as an active heat transfer shunt to maintain the temperature gradient across the top square as close to zero as possible. Unfortunately, similar to the first prototype, the performance of this system did not justify additional refinement.

As mentioned previously, the third prototype, Figure C-3, created all of the experimental data in this thesis. A simple twinned design built with disposable stereolithography microfluidic cells was used to perform the RNase A protein experiments documented in Figures 5-1-5-2. Note that the geometry characteristics of the cell are similar to the first prototype. The intention of the design was to ensure that conduction was the dominant heat transfer pathway. However, the author failed to recalculate the appropriate geometric sizes considering the thermal properties of the polymer instead of 316 stainless. Notice the similarity in the geometric design fea-

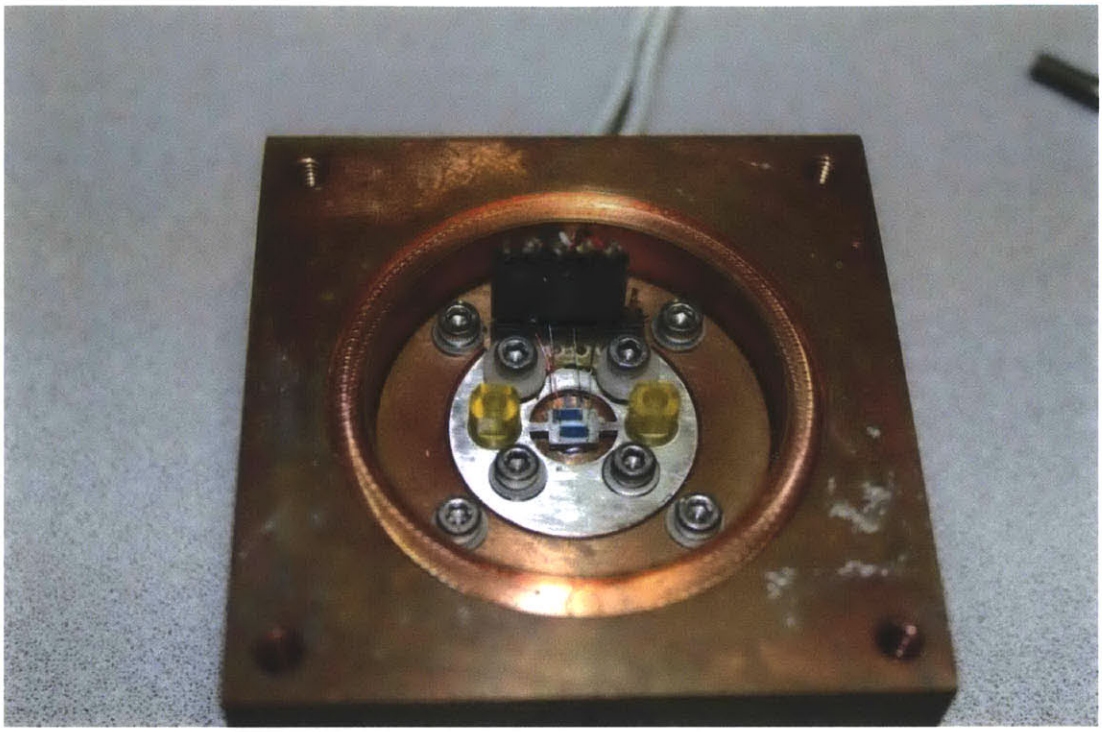

Figure C-1: First generation prototype calorimeter.

tures of prototypes one and three. As a result, while validating the model discussed in Section 3.3, initially the fitted thermal resistances appeared too low for the calculated values. This was due to an incorrect assumption that conduction was the dominant heat transfer mode. However, after convective resistances were calculated, they matched the fitted experimental results.

The fourth prototype, Figure C-4 is still being built. In has a similar design to the third prototype except geometry has been changed to try and ensure that conduction is the dominant heat transfer pathway. The purpose of designing for only conductive heat transfer is to minimize the impact of ambient disturbances through a leakage path that is not controlled through temperature feedback control.

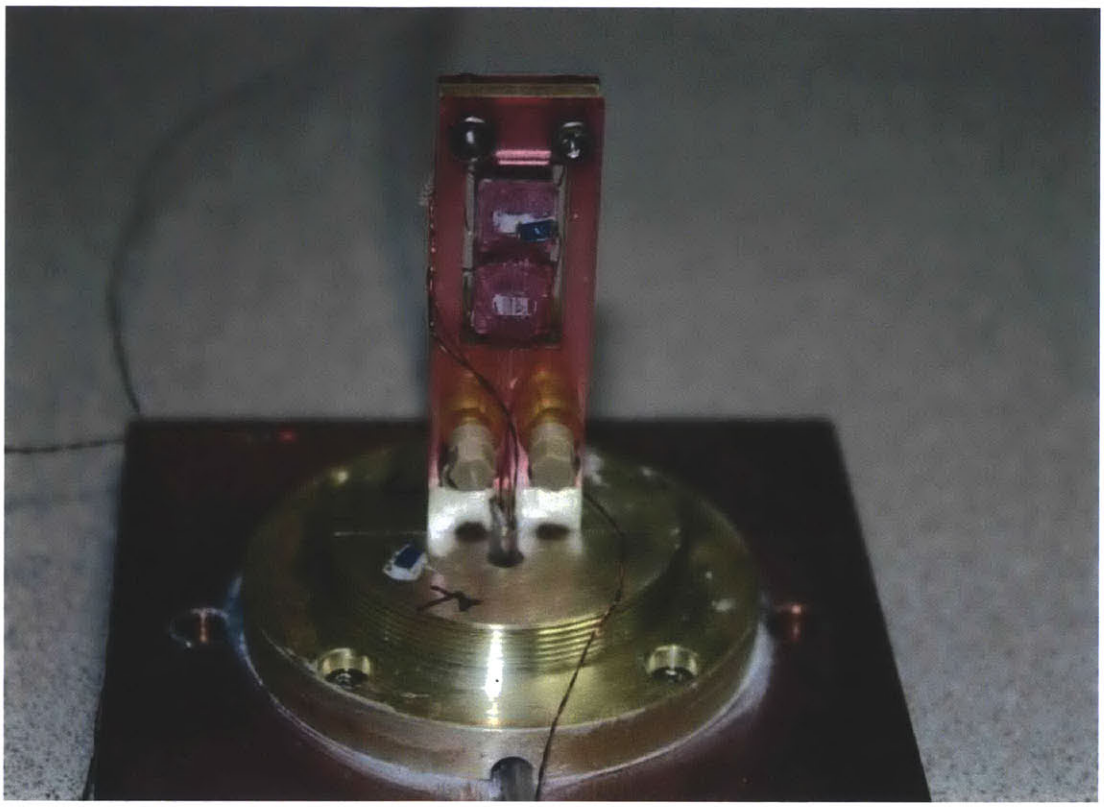

Figure C-2: Second generation prototype calorimeter.

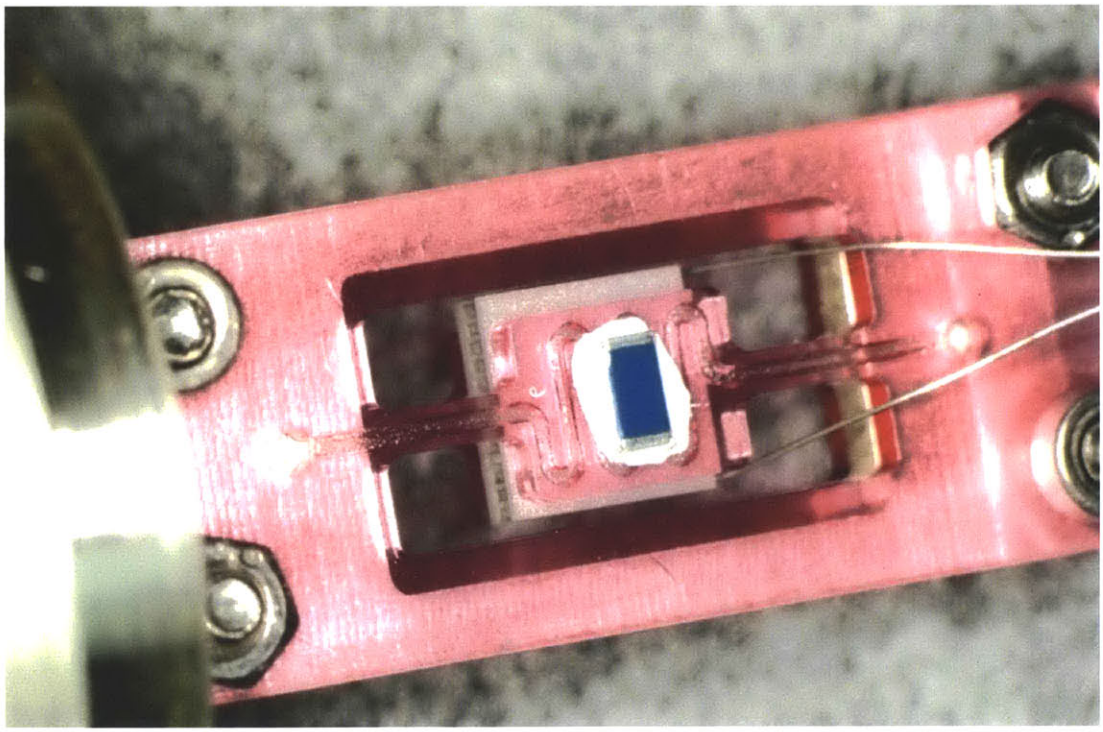

Figure C-3: Third generation prototype calorimeter.

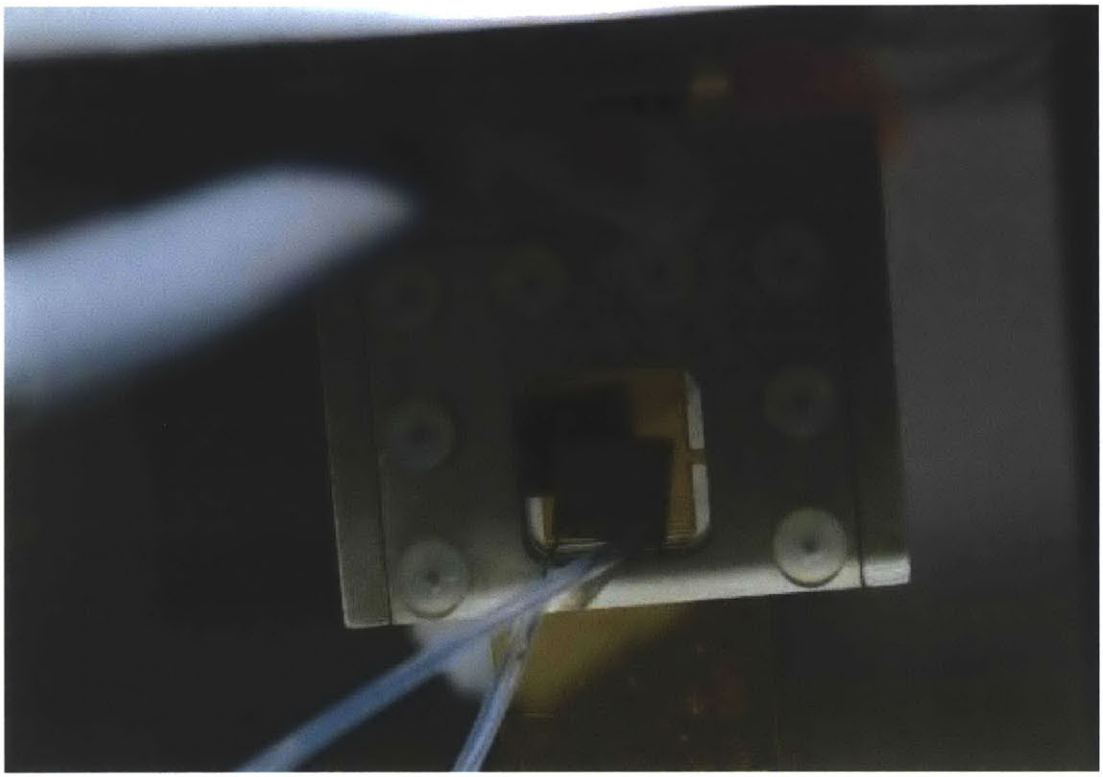

Figure C-4: Fourth generation prototype calorimeter.

Bibliography

[1] A revolution in r&d: How genomics and genetics are transforming the biopharmaceutical indsutry. Technical report, Boston Consulting Group, 2001.

[2] Ieee standard for digitizing waveform recorders, 2007.

[3] Ieee standards for for terminology and test methods for analog-to-digital converters, 2010.

[4] Fda glossary of terms, April 2013.

[5] Ge healthcare vp capillary data analysis manual. Technical report, GE Healthcare, 2013.

[6] V. Baier, R. Fdisch, A. Ihring, E. Kessler, J. Lerchner, G. Wolf, J.M. Khler, M. Nietzsch, and M. Krgel. Highly sensitive thermopile heat power sensor for micro-fluid calorimetry of biochemical processes. *Sensors and Actuators A: Physical*, 123-124:354–359, 2005.

[7] R. Berger, Ch. Gerber, J. K. Gimzewski, E. Meyer, and H. J. Guntherodt. Thermal analysis using a micromechanical calorimeter. *Applied Physics Letters*, 69(1):40–42, 1996.

[8] E. B. Chancellor, J. P. Wikswo, F. Baudenbacher, M. Radparvar, and D. Osterman. Heat conduction calorimeter for massively parallel high throughput measurements with picoliter sample volumes. *Appl. Phys. Lett.*, 85(12):2408–2410, September 2004.

[9] R. David and I. Hunter. A liquid expansion microcalorimeter. *Journal of Thermal Analysis and Calorimetry*, 90(2):597–599, 2007.

[10] Michael Dickson and Jean Paul Gagnon. The cost of new drug discovery and development. *Discovery Medicine*, 37, 2009.

[11] J.K. Gimzewski, Ch. Gerber, E. Meyer, and R.R. Schlittler. Observation of a chemical reaction using a micromechanical sensor. *Chemical Physics Letters*, 217(5-6):589 – 594, 1994.

[12] G.W.H. Hohne and W. Winters. About models and methods to describe chip-calorimeters and determine sample properties from the measured signal. *Thermochimica Acta*, 432(2):169 – 176, 2005. ¡ce:title¿Thermodynamics and calorimetry of thin films: Papers presented at the 8th Lhnwitzseminar on Calorimetry¡/ce:title¿ ¡xocs:full-name¿Thermodynamics and calorimetry of thin films: Papers presented at the 8th Lhnwitzseminar on Calorimetry¡/xocs:full-name¿.

[13] Ian Hunter. Electro-mechanical system: Stochastic binary input. Technical report, Massachusett Institute of Technology, 2009.

[14] E. Iervolino, A.W. van Herwaarden, and P.M. Sarro. Calorimeter chip calibration for thermal characterization of liquid samples. *Thermochimica Acta*, 492(1-2):95–100, August 2009.

[15] Erik A. Johannessen, John M. R. Weaver, Lenka Bourova, Petr Svoboda, Peter H. Cobbold, and Jonathan M. Cooper. Micromachined nanocalorimetric sensor for ultra-low-volume cell-based assays. *Analytical Chemistry*, 74(9):2190–2197, May 2002.

[16] Walter G. Jung. Op amp applications. Technical report, Analog Devices Inc., 2002.

[17] Wonhee Lee, Warren Fon, Blake W. Axelrod, and Michael L. Roukes. High-sensitivity microfluidic calorimeters for biological and chemical applications. *Proceedings of the National Academy of Sciences*, 106:15225–15230, 2009.

[18] J. Lerchner, A. Wolf, and G. Wolf. Recent developments in integrated circuit calorimetry. *Journal of Thermal Analysis and Calorimetry*, 57(1):241–251, 1999.

[19] Johannes Lerchner, Thomas Maskow, and Gert Wolf. Chip calorimetry and its use for biochemical and cell biological investigations. *Chemical Engineering and Processing: Process Intensification*, 47(6):991–999, June 2008.

[20] Brad Lubbers and Franz Baudenbacher. Isothermal titration calorimetry in nanoliter droplets with subsecond time constants. *Analytical Chemistry*, 83(20):7955–7961, 2011.

[21] I. R. Mckinnon, L. Fall, A. Parody-Morreales, and S. J. Gill. A twin titration microcalorimeter for the study of biochemical reactions. *Analytical Biochemistry*, 139(1):134–139, 1984.

[22] Rick Ng. *Drugs from Discovery to Approval.* Wiley-Blackwell, 2009.

[23] Michiel A. P. Pertijs and Johan H. Huijsing. *PRECISION TEMPERATURE SENSORS IN CMOS TECHNOLOGY.* Springer, 2006.

[24] P. L. Privalov and V. V. Plotnikov. 3 generations of scanning microcalorimeters for liquids. *Thermochimica Acta*, 139:257–277, 1989.

[25] Ronald A. Rader. Fda biopharmaceutical product aapproval and trends: 2012. Technical report, Biotechnology Information Institute, 2012.

[26] Michael I. Recht, Dirk De Bruyker, Alan G. Bell, Michal V. Wolkin, Eric Peeters, Greg B. Anderson, Anand R. Kolatkar, Marshall W. Bern, Peter Kuhn, Richard H. Bruce, and Frank E. Torres. Enthalpy array analysis of enzymatic and binding reactions. *Analytical Biochemistry*, 377:33–39, 2008.

[27] R. B. Spokane and S. J. Gill. Titration microcalorimeter using nanomolar quantities of reactants. *Rev. Sci. Instrum.*, 52(11):1728–1733, November 1981.

[28] R. Mark Stitt. Make a precision current source or current sink. Technical report, Burr-Brown Application Bulletin, 1994.

[29] Michael C. Swiontek and Rolly Hassun. The linear quartz thermometer - a new tool for measuring absolute and difference temperatures. *Hewlett-Packard Journal*, 16:1–12, 1965.

[30] Francisco E. Torres, Peter Kuhn, Dirk De Bruyker, Alan G. Bell, Michal V. Wolkin, Eric Peeters, James R. Williamson, Gregory B. Anderson, Gregory P. Schmitz, Michael I. Recht, Sandra Schweizer, Lincoln G. Scott, Jackson H. Ho, Scott A. Elrod, Peter G. Schultz, Richard A. Lerner, , and Richard H. Bruce. Enthalpy arrays. *Proceedings of the National Academy of Sciences*, 101:9517–9522, 2004.

[31] Katarina Verhaegen, Kris Baert, Jeannine Simaels, and Willy Van Driessche. A high-throughput silicon microphysiometer. *Sensors and Actuators A: Physical*, 82(1-3):186–190, May 2000.

[32] Gary Walsh. Biopharmaceutical benchmarks 2006. *Nature Biotechnology*, 24:769–776, 2006.

[33] Bin Wang and Qiao Lin. A mems differential-scanning-calorimetric sensor for thermodynamic characterization of biomolecules. *Microelectromechanical Systems, Journal of*, 21(5):1165–1171, 2012.

[34] Li Wang, David M. Sipe, Young Xu, and Qiao Lin. A mems thermal biosensor for metabolic monitoring applications. *Journal of Microelectromechanical Systems*, 17:318–327, 2008.

[35] Li Wang, Bin Wang, and Qiao Lin. Demonstration of mems-based differential scanning calorimetry for determining thermodynamic properties of biomolecules. *Sensors and Actuators B: Chemical*, 134(2):953 – 958, 2008.

[36] S. Wang, K. Tozaki, H. Hayashi, and H. Inaba. Nano-watt stabilized dsc and its applications. *Journal of Thermal Analysis and Calorimetry*, 79:605–613, 2005.

[37] Werner Winter and G. W.H Hohne. Chip-calorimeter for small samples. *Thermochimica Acta*, 403(1):43 – 53, 2003. ¡ce:title¿Thermodynamics and Calorimetry of Small Systems Papers Presented at the 7th Laehnwitzseminar on Calorimetry¡/ce:title¿.

[38] T Wiseman, S Williston, JF Brandts, and LN Lin. Rapid measurement of binding constants and heats of binding using a new titration calorimeter. *Analytical Biochemistry*, 179(1):131–137, 1989.

[39] Bernhard Wunderlich. *Thermal Analysis.* Academic Press, 1990.

[40] Junkai Xu, Ron Reiserer, Joel Tellinghuisen, John P. Wikswo, and Franz J. Baudenbacher. A microfabricated nanocalorimeter: Design, characterization, and chemical calibration. *Analytical Chemistry*, 80(8):2728–2733, April 2008.

[41] Yuyan Zhang and Srinivas Tadigadapa. Calorimetric biosensors with integrated microfluidic channels. *Biosensors and Bioelectronics*, 19(12):1733–1743, July 2004.

[42] J. G. Ziegler and N. B. Nichols. Optimum settings for automatic controllers. *Transaction of the ASME*, 64:759–768, 1942.